Egypt. J. Chem. **Vol. 68,** No. 7 pp. 457 – 481 (2025)

Egyptian Journal of Chemistry

http://ejchem.journals.ekb.eg/

Novel heterocyclic Schiff base ligand and its metal complexes: Synthesis, characterization, molecular docking and DFT

Mahmoud N. Anwar[1*], M. Khodari[4], A.A. Ebnelwaled[4], Walla H. Mahmoud[2], Gehad G. Mohamed[2,3*]

[1] *El-Nasr Co. for intermediate Chemicals, Giza, Egypt*
[2] *Chemistry Department, Faculty of Science, Cairo University, Giza, 12613, Egypt*
[3] *Nanoscience Department, Institute of Basic and Applied Sciences, Egypt-Japan University of Science and Technology, New Borg El Arab, Alexandria, 21934, Egypt*
[4] *Chemistry Department, Faculty of Science, South Valley University, Qena, 83523, Egypt*

Abstract

This study presents the synthesis, characterization, and diverse applications of novel Schiff base (L) metal complexes derived from quinoline-2-carboxaldehyde and 3-amino-1,2,4-triazole. A series of complexes with various transition metals, including Cu(II) and Fe(III), were successfully synthesized and thoroughly characterized using analytical techniques. These techniques included elemental analysis, spectroscopic methods (FT-IR, NMR, UV-Vis), and thermal analysis, providing comprehensive insights into their structural and physicochemical properties. The research employed advanced computational techniques, such as density functional theory (DFT) calculations, to further elucidate these complexes' electronic structures and properties. Molecular docking studies were conducted to explore potential interactions with biological targets, offering valuable insights into their possible mechanisms of action in biological systems. A significant focus of the study was the investigation of these complexes' antimicrobial properties against a range of bacterial and fungal strains, revealing promising activities that suggest potential applications in medicinal chemistry. The morphological and textural characteristics of selected complexes, particularly those of Cu(II) and Fe(III), were extensively examined using advanced microscopy techniques and surface area analysis, uncovering their nanoscale features and high surface areas. The research further explored the environmental applications of these nanocomplexes, demonstrating their efficacy in two key areas: the electrochemical detection of arsenic and the adsorptive removal of organic dyes from aqueous solutions. Detailed studies on the adsorption behavior, including pH and contact time effects, were conducted to optimize their performance in water treatment applications. Additionally, the reusability of these materials was assessed, providing important insights into their potential for practical, long-term use in environmental remediation processes. This comprehensive study contributes significantly to the growing field of multifunctional metal complexes, highlighting their versatility and potential in addressing various environmental, analytical, and biological challenges. The findings open new avenues for developing advanced materials with applications ranging from water purification to antimicrobial agents and chemical sensors.

Keywords: nanometal; complexes; DFT; docking; biological activity; cyclic voltammetry; dye removal.

1. Introduction

Schiff bases, discovered by Hugo Schiff in 1864, are a significant class of organic compounds characterized by an imine group (-C=N-). These versatile substances are formed through the condensation of primary amines with aldehydes or ketones. Schiff bases have gained considerable attention in chemistry due to their diverse structural possibilities and their remarkable ability to form stable complexes with various metal ions. This property has made them valuable in coordination chemistry, catalysis, and materials science. Their adaptability and unique chemical characteristics have led to widespread applications across multiple fields, from synthetic organic chemistry to medicinal research, highlighting their ongoing importance in modern scientific endeavors [1]. The versatility of Schiff bases as ligands is rooted in their ability to coordinate metals via nitrogen atoms from the imine group and, in some cases, through oxygen or sulfur atoms as additional donor sites. This coordination behavior makes Schiff bases crucial in coordination chemistry, where their metal complexes are of interest for various applications in catalysis, materials science, and biomedicine [2]. Metal complexes of Schiff bases are particularly noteworthy due to their stability and diverse geometries, often leading to enhanced chemical reactivity and potential for practical applications. Transition metals such as copper, cobalt, nickel, and iron form stable complexes with Schiff bases, adopting coordination geometries like square planar, tetrahedral, or octahedral, depending on the metal centre and the ligand environment. These metal complexes are well-known for their ability to act as catalysts in necessary organic transformations, such as oxidation, reduction, and polymerization reactions. Their catalytic efficiency is often superior to that of uncomplexed Schiff bases, primarily due to the enhanced reactivity imparted by the metal ions [3]. Apart from their industrial applications, Schiff base metal complexes are recognized for their significant biological activities. Numerous studies have demonstrated that these complexes possess antimicrobial, antifungal, anticancer, and antioxidant properties. Their ability to interact with biological

*Corresponding author e-mail: mahmoudnoshy@gstd.sci.cu.edu.eg (Mahmoud N. Anwar).
Receive Date: 04 October 2024, **Revise Date:** 14 November 2024, **Accept Date:** 04 December 2024
DOI: https://doi.org/10.21608/ejchem.2024.325904.10575

macromolecules, such as DNA and proteins, is central to their pharmacological potential. Introducing metal ions into the Schiff base framework often leads to improved biological activity, as the metal center can enhance the ligand's ability to permeate cell membranes, increase bioavailability, and improve interactions with biological targets [4]. Schiff base metal complexes have been widely investigated as potential therapeutic agents, with some showing promising results in developing drugs to combat resistant bacterial strains and various forms of cancer [5]. Density Functional Theory (DFT) is a key computational method used to study Schiff base metal complexes. It allows researchers to model molecular structures, calculate electronic properties, and predict spectroscopic behaviors. DFT complements experimental work by providing insights into metal-ligand interactions, charge distributions, and reaction mechanisms. This approach aids in designing new complexes and interpreting experimental data, advancing our understanding of these compounds in various scientific fields. DFT provides a detailed quantum mechanical analysis of these complexes, allowing researchers to predict their electronic structure, geometry, and reactivity. This theoretical approach aids in understanding how the metal center and Schiff base ligand interact at the atomic level, and it plays a critical role in designing new complexes with tailored properties for specific applications [6]. DFT studies have become invaluable in predicting the behavior of these complexes in catalytic reactions and their stability in biological systems [7]. In addition to DFT, molecular docking studies are commonly used to investigate the interaction between Schiff base metal complexes and biological targets, such as enzymes and receptors. Docking simulations provide insights into the binding affinities and interaction modes of the complexes with biomolecules, helping researchers understand the potential of these compounds as therapeutic agents [8]. These studies are instrumental in drug discovery, as they allow for the rational design of Schiff base metal complexes with enhanced biological activity and specificity towards their targets [9]. Researchers can bridge the gap between theoretical predictions and experimental observations by combining DFT and molecular docking techniques, thereby accelerating the development of Schiff base-based catalysts and pharmaceuticals [10]. Triazoles have recently emerged as significant heteroaromatic compounds, widely used as versatile ligands in inorganic synthesis. Their importance stems from a broad spectrum of biological activities, including antimicrobial, antifungal, antitumor, anticancer, antibacterial, anticonvulsant, analgesic, and insecticidal properties. This diverse range of effects has made triazoles valuable in medicinal chemistry and agrochemical research, driving continued interest in their development and applications [11 – 15]. Cyclic voltammetry (CV) is a powerful electrochemical technique that has become increasingly important in studying Schiff base metal complexes. This method provides valuable insights into the redox properties, electron transfer kinetics, and stability of these complexes [16]. In CV, the potential of a working electrode is cycled linearly with time between two or more set potentials, and the resulting current is measured. This technique allows researchers to observe the oxidation and reduction processes of the metal centers and ligands, providing information about the electrochemical behavior of the complexes. CV has been particularly useful in investigating the potential applications of Schiff base metal complexes in electrochemical sensing, catalysis, and energy storage devices. The characteristic voltammograms obtained from CV measurements can reveal the number of electrons involved in redox processes, the reversibility of these processes, and the presence of any intermediate species. This information is crucial for understanding the electronic structure and reactivity of Schiff base metal complexes, complementing the insights gained from spectroscopic and computational studies [17]. This study aimed to synthesize a Schiff base ligand from the condensation of quinoline-2-carboxaldehyde and 3-Amino-1,2,4-triazole and explore its metal complexes. The resulting Schiff base metal complexes were structurally characterized using various analytical techniques to provide insight into their structural and chemical properties and confirm their stability and reactivity. A key objective was to employ Density Functional Theory (DFT) calculations to elucidate the electronic structure, molecular geometry, and reactivity of the synthesized Schiff base ligand and its metal complexes. This aimed to provide deeper insights into metal-ligand interactions and factors influencing stability and reactivity. Additionally, comprehensive molecular docking analyses were conducted to investigate potential interactions between the synthesized compounds and various biological targets, including proteins involved in cancer cell cycles, viral infections, and enzymes from pathogenic organisms. By combining DFT calculations with molecular docking simulations, we sought to establish structure-activity relationships and predict potential biological activities [18]. The study also focused on evaluating the antimicrobial properties of these complexes against both Gram-positive and Gram-negative bacteria and their antifungal activity. Furthermore, the research explored potential applications in environmental remediation, particularly in the detection and removal of pollutants such as arsenic and organic dyes from aqueous solutions. This included investigating the electrochemical properties through cyclic voltammetry for arsenic detection and studying adsorption capabilities for Rose Bengal dye removal, with an emphasis on optimizing conditions and assessing reusability. Through this multifaceted approach, we aimed to provide a comprehensive understanding of these novel Schiff base metal complexes and their potential applications in medicinal chemistry and environmental science.

2. Experimental

2.1. Material and reagents

The study employed a range of high-purity chemicals from various suppliers. The primary organic compound, 3-Amino-1,2,4-triazole ($C_2H_4N_4$), was obtained from Alfa Aesar. A series of metal chloride hydrates were utilized, with $CrCl_3 \cdot 6H_2O$ and $MnCl_2 \cdot 2H_2O$ sourced from Sigma, while $FeCl_3 \cdot 6H_2O$ was procured from Prolabo. The remaining metal chlorides, including $CoCl_2 \cdot 6H_2O$, $NiCl_2 \cdot 6H_2O$, $CuCl_2 \cdot 2H_2O$, $ZnCl_2 \cdot 2H_2O$, and $CdCl_2$, were all supplied by BDH. For the solvents, the researchers used dimethylformamide (DMF, C_3H_7NO) at 97% purity and ethanol (C_2H_5OH) at both 99% and 95% concentrations, all provided by Adwic. Deionized water (H_2O) was produced in-lab using glass distillation equipment to ensure the highest purity level in aqueous preparations. Rose Bengal dye, sodium hydroxide, arsenic trioxide (As_2O_3), and sodium

dihydrogen arsenate were procured from Sigma-Aldrich. This comprehensive selection of chemicals from reputable sources ensured the integrity and reliability of the experimental procedures throughout the study.

2.2 Measurements Analytical Techniques

The microanalysis for carbon, hydrogen, and nitrogen was performed at the Microanalytical Center of Cairo University, Egypt, utilizing a CHNS–932 (LECO) Vario Elemental Analyzer. Metal content in the complexes was determined after dissolving the solid complexes in hot concentrated nitric acid, neutralizing the diluted aqueous solutions with ammonia, and titrating with EDTA. The FT-IR spectra were recorded on a Perkin-Elmer 1650 spectrometer within the 4000 to 400 cm^{-1} range using KBr pellets. The ^{1}H-NMR spectra, prepared in DMSO-d^6 solution, were recorded at room temperature on a Varian – Oxford Mercury 400 MHz "NMR 400" instrument, with TMS as an internal standard. Molar conductivities of 10^{-3} M solutions of the solid complexes in DMF were measured with a Jenway 4010 conductivity meter. Melting points were determined using a Stuart SMP 30 melting point apparatus from the U.K. The molar magnetic susceptibility of powdered samples was measured using the Faraday method, with diamagnetic corrections applied using Pascal's constant, and $Hg[Co(SCN)_4]$ was used as a calibrant. UV-visible spectra were recorded using a Shimadzu UVmini-1240 UV-Vis spectrophotometer.

3. Synthesis of Schiff Base Ligand and Metal Complexes

3.1. Synthesis of Schiff Base Ligand

The Schiff base ligand (L) was synthesized through a condensation reaction between quinoline-2-carboxaldehyde and 3-amino-1,2,4-triazole. To initiate the reaction, 4.5 g (0.0287 mol) of quinoline-2-carboxaldehyde was dissolved in dimethylformamide (DMF). This solution was combined with 2.41 g (0.0287 mol) of 3-amino-1,2,4-triazole, previously dissolved in ethanol. The resulting mixture underwent reflux conditions for 2 hours. Following the reaction, the product precipitated out of solution. This solid was isolated via filtration, thoroughly washed with ethanol to remove impurities, and dried. The mass of the final product was measured, revealing an impressive yield of 95%. The overall synthetic pathway and the structural representation of the resulting Schiff base ligand were illustrated in Scheme 1. This reaction exemplifies a typical imine formation, where the aldehyde group of quinoline-2-carboxaldehyde condenses with the primary amine of 3-amino-1,2,4-triazole, eliminating water in the process to form the characteristic C=N bond of a Schiff base.

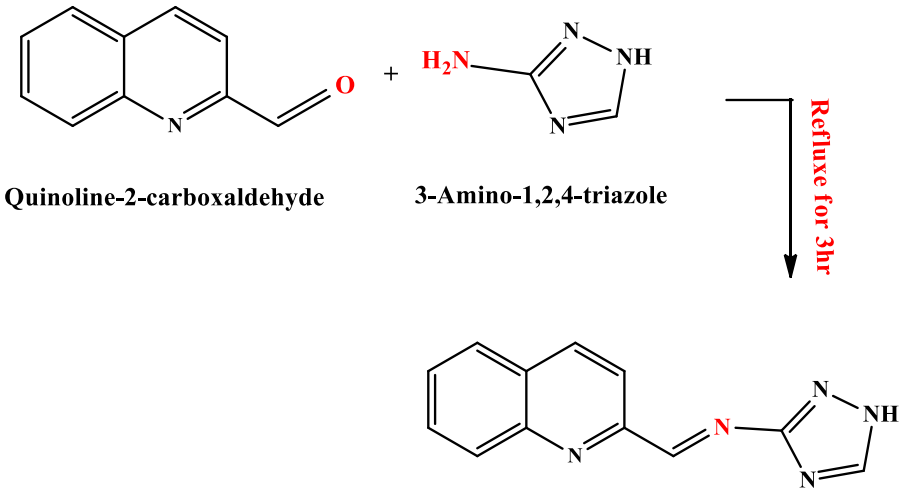

Quinoline-2-carboxaldehyde **3-Amino-1,2,4-triazole**

(*E*)-1-(quinolin-2-yl)-*N*-(1*H*-1,2,4-triazol-3-yl)methanimine

Schiff base ligand (L)

Scheme 1. Synthesis pathway of (L)

3.2. Synthesis of Schiff base metal complexes

The synthesis of metal complexes with the Schiff base ligand **(L)** involved a series of reactions with various metal chloride salts. Initially, 0.5 g (0.00224 mmol) of the Schiff base ligand **(L)** was dissolved in 40 mL of C_2H_5OH. This solution was then combined with ethanolic solutions of different metal chloride salts, each prepared by dissolving 0.00112 mmol (half the molar amount of the ligand) of the respective salt in 20 mL of C_2H_5OH, reflecting a 2:1 ligand-to-metal ratio. The metal salts used in these reactions included $CrCl_3 \cdot 6H_2O$ (0.297 g), $MnCl_2 \cdot 2H_2O$ (0.180 g), $FeCl_3 \cdot 6H_2O$ (0.302 g), $CoCl_2 \cdot 6H_2O$ (0.266

g), $NiCl_2 \cdot 6H_2O$ (0.265 g), $CuCl_2 \cdot 2H_2O$ (0.190 g), $ZnCl_2 \cdot 2H_2O$ (0.153 g), and $CdCl_2$ (0.205 g), each at 0.00112 mmol. The mixtures were stirred at room temperature for one hour and refluxed for 3 hours. This process yielded colored precipitates, which were isolated by filtration, washed with C_2H_5OH to remove impurities, dried, and weighed. The yields of these complexes are recorded in Table 2. Scheme 2 illustrated the general synthetic pathway for these metal complexes, showing the coordination of two Schiff base ligands to each metal center. This approach highlights the bidentate nature of the ligand and its ability to form bis-complexes with various transition metals, potentially resulting in compounds with interesting structural and electronic properties.

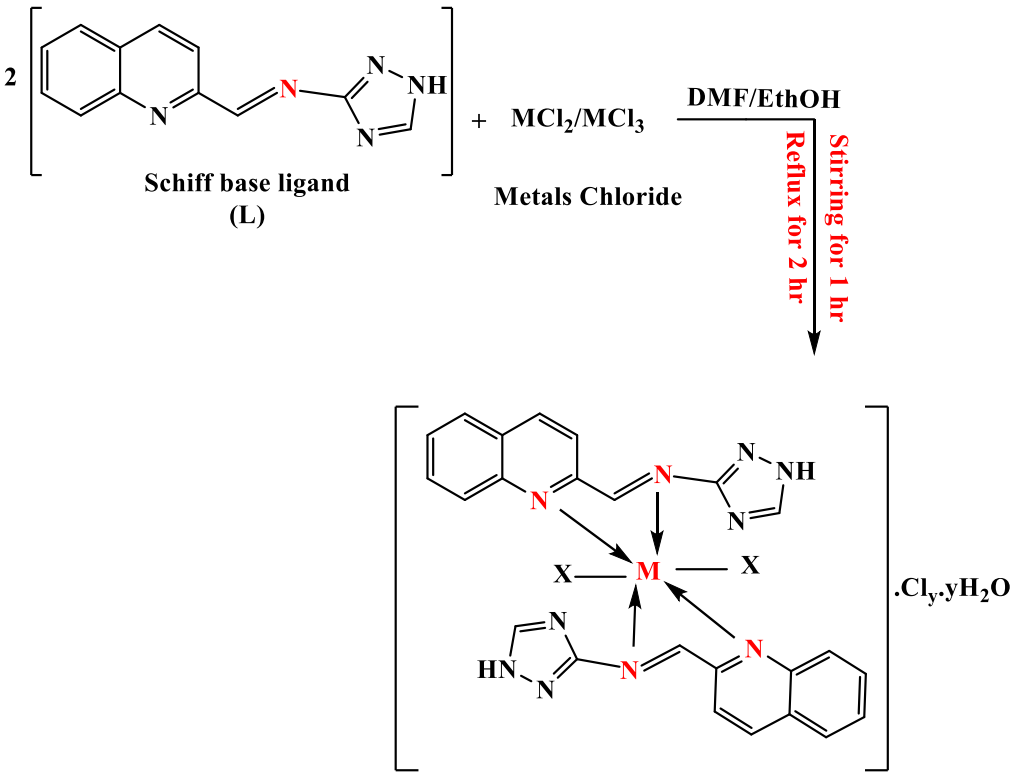

Scheme 2. General reaction of synthesis of metal complexes of Schiff base ligand (L), M = Cr(III), Mn(II), Fe(III), Co(II), Ni(II), Cu(II), Zn(II) and Cd(II), x = Cl or H_2O and y = No. of Cl or H_2O.

3.3 Absorption spectra of the (L) and its metal complexes

The absorption spectra of a $1^{x}10^{-4}$ M solution of the Schiff base ligand **(L)** and the investigated metal complexes were measured in the DMF solvent. The measurements were taken in the wavelength range of 200 to 700 nm.

3.4 Antimicrobial Assay Procedure

The antimicrobial activity of the compounds was evaluated using the agar well diffusion method. The test subjects included Gram-positive bacteria (*Staphylococcus aureus* and *Streptococcus mutans*), Gram-negative bacteria (*Escherichia coli*, *Pseudomonas aeruginosa*, and *Klebsiella pneumonia*), and fungi (*Candida albicans* and *Asperagillus niger*). Nutrient agar medium was used for bacteria, while Sabouraud dextrose agar medium was used for fungi. Ampicillin and Gentamicin served as standard drugs for Gram-positive and Gram-negative bacteria, respectively, with Nystatin as the standard for fungi. DMSO was employed as a negative control. The compounds were tested at 15 mg/ml concentration. The procedure involved preparing microbial suspensions (1.5^{x} 105 CFU mL^{-1}), inoculating agar plates, creating wells in the media, and adding 100 µL of test compound solutions. Plates were incubated at 37°C for 24 hours for antibacterial activity. The experiment was performed in triplicate, with zones of inhibition measured in millimeters [19]. Statistical analysis was conducted using one-way ANOVA and Duncan multiple comparisons test, with $p<0.05$ considered statistically significant.

3.5. Computational methodology

The electronic structure of the Schiff base ligand (L) and its metal complexes was analyzed using the Gaussian09 software [20]. Full optimization of the structures was achieved with density functional theory (DFT) employing the hybrid B3LYP functional. A mixed basis set approach was utilized to model the system accurately: the LANL2DZ basis set was applied to the Cu and Fe atoms, suitable for transition metals, while the 6-31G(d,p) basis set was used for the ligand atoms (C, H, N, O) in both the ligand (L) and its Cu(II) and Fe(III) complexes, ideal for main group elements. This combination facilitated the geometry optimization and allowed for the calculation of various functional parameters such as Total Energy, Dipole Moment, E_{HOMO}, E_{LUMO}, Band Gap Energy ($\Delta E = E_{HOMO} - E_{LUMO}$), Electron Affinity, Electronegativity, and Electrostatic Maps (MEP) [21, 22]. The optimized molecular electrostatic potential (MEP) identified the reactive sites within the molecule, particularly highlighting regions of electrophilic reactivity characterized by negative potential.

3.6. Molecular docking study

Molecular docking analyses were performed using MOE 2014 software, known for its robust molecular docking capabilities [22, 23]. These analyses were essential in predicting the potential binding modes of the Schiff base ligand (L) and its metal complexes with key biological receptors. The three-dimensional structures of the target proteins were obtained from the Protein Data Bank (PDB). The optimal structures of the complexes were generated using Gaussian 09 software with the B3LYP method and subsequently docked to the target receptors using MOE. The docking studies focused on identifying potential binding interactions with proteins involved in various biological processes, including the cancer cell cycle (7DAE), the immune system and viral proteins (6W41, associated with COVID-19), and enzymes from pathogenic organisms such as *Candida albicans* (hydrolase/5JPE), *Staphylococcus aureus* (hydrolase/1GHP, ligase/jij, tyrosyl-tRNA synthetase/1JIL), *Streptococcus mutans* (transferase/3AIC, dextran glucosidase/2ZIC), *Pseudomonas aeruginosa* (transcriptional activator protein lasr/3IX3), *Neisseria gonorrhoeae* (membrane proteins/5WAQ, 5WAM), and *Bacillus subtilis* (protein HFQ/3AHU). These analyses provided insights into the potential efficacy of the Schiff base ligand and its complexes in targeting these proteins.

4. Result and Discussion

4.1. Microanalysis of Metal Complexes

The microanalysis results provided crucial information about the composition and properties of the synthesized metal complexes. Elemental analyses for carbon, hydrogen, and nitrogen were conducted, and the results were compiled in Table 2 alongside the compounds' molecular formulas and physical properties. The data revealed that all complexes exhibited a 1:2 metal-to-ligand stoichiometry, confirming the formation of ML_2 type complexes. This composition was consistent across all the metal complexes synthesized, regardless of the specific transition metal used. These complexes demonstrated stability at ambient temperature, indicating their potential for practical applications without special storage conditions. Regarding solubility, the complexes showed limited solubility in C_2H_5OH but were readily soluble in polar aprotic solvents such as C_3H_7NO (DMF) and $(CH_3)_2SO$ (DMSO). This solubility profile suggests that these solvents would be suitable for further characterization or application of the complexes. Notably, the experimental results from the elemental analyses closely matched the theoretical values calculated based on the proposed molecular formulas. This agreement between observed and calculated values provides strong support for the suggested structures of the complexes, reinforcing the validity of the synthetic approach and the resulting ML_2 complex formation.

4.2. Molar Conductivity Analysis of Metal Complexes

Molar conductivity measurements of metal complexes in DMF at room temperature revealed two distinct groups. Mn(II), Co(II), Zn(II), and Cd(II) complexes showed low conductivity, indicating their non-ionic, non-electrolytic nature. Conversely, Cr(III), Fe(III), Ni(II), and Cu(II) complexes displayed conductivity values of 70-60 Ω^{-1} mol^{-1} cm^2, suggesting ionic character and classifying them as 1:1 electrolytes. These findings provide crucial insights into the ionic behavior of the synthesized complexes in solution, which is important for understanding their potential applications and reactivity in various systems (Table 1).

Table 1: Analytical and physical properties of the Schiff base ligand (L) and its metal complexes

Compound	%yield	MP °C	Λ Ω^{-1} mol^{-1} cm^2	$\mu_{eff.}$ B.M.	Found (Calcd. %)			
					C	H	N	M
L	97.00	210	----	Diamagnetic	64.35 (64.57)	3.89 (4.04)	30.77 (31.39)	-----
$[Cr(L)_2Cl_2]Cl.4H_2O$	91.35	250	70.0	4.75	42.29 (42.57)	3.66 (3.84)	20.38 (20.69)	7.52 (7.69)
$[Mn(L)_2Cl_2].3H_2O$	86.45	240	4.50	5.51	45.89 (46.10)	3.54 (3.84)	22.18 (22.40)	8.24 (8.64)
$[Fe(L)_2Cl_2]Cl.4H_2O$	86.88	255	60.0	5.10	42.16 (42.32)	3.43 (3.82)	20.22 (20.57)	7.87 (8.23)
$[Co(L)_2Cl_2].2H_2O$	88.25	240	5.10	5.78	46.98 (47.14)	3.44 (3.60)	22.56 (22.91)	9.19 (9.49)
$[Ni(L)_2(H_2O)Cl]Cl.H_2O$	93.40	220	70.0	3.95	46.88 (46.91)	3.22 (3.58)	22.43 (22.80)	9.32 (9.93)
$[Cu(L)_2(H_2O)Cl]Cl.2H_2O$	90.00	220	50.00	1.65	45.14 (45.43)	3.54 (3.79)	21.82 (22.10)	9.43 (9.94)
$[Zn(L)_2Cl_2].3H_2O$	91.54	230	12.0	Diamagnetic	45.13 (45.28)	3.52 (3.51)	21.86 (22.00)	10.06 (10.22)
$[Cd(L)_2Cl_2].3H_2O$	87.45	260	10.0	Diamagnetic	42.06 (42.17)	3.31 (3.51)	20.42 (20.50)	16.14 (16.39)

4.3. UV-Visible Spectral Analysis

The electronic absorption spectra of the Schiff base ligand (L) and its metal complexes were recorded in DMF solution in the range of 200-700 nm (Supplementary Figure S1). The free ligand (L) exhibits two main absorption bands: a high-intensity band at 266 nm attributed to π→π* transitions of the aromatic rings and azomethine chromophore, and a lower intensity band at 316 nm assigned to n→π* transitions involving the lone pair of electrons on the nitrogen atoms [18-21]. Upon metal complexation, these bands undergo characteristic modifications. The Cr(III) complex shows bathochromic shifts with bands at 276 nm (π→π*) and 325 nm (n→π*), accompanied by a ligand-to-metal charge transfer (LMCT) band at 380 nm and a d-d transition band at 520 nm assigned to $^2Eg \rightarrow {}^2T2g$ transition. The Mn(II) complex exhibits absorption peaks at 282 nm (π→π*) and 332 nm (n→π*), with a metal-to-ligand charge transfer (MLCT) band at 375 nm and a characteristic d-d transition at 545 nm corresponding to $^6A1g \rightarrow {}^4T1g$ transition [38, 39]. The Fe(III) complex displays enhanced absorption bands at 286 nm (π→π*) and 348 nm (n→π*), along with an LMCT band at 385 nm and a d-d transition at 535 nm attributed to $^6A1g \rightarrow {}^4T2g$ transition. The Co(II) complex demonstrates shifts to 280 nm (π→π*) and 335 nm (n→π*), featuring an MLCT band at 370 nm and a d-d transition at 550 nm assigned to $^4T1g \rightarrow {}^4T2g$ transition. The Ni(II) complex shows absorption bands at 278 nm (π→π*) and 330 nm (n→π*), with a distinctive d-d transition at 565 nm corresponding to $^3A2g \rightarrow {}^3T1g$ transition. The Cu(II) complex exhibits significant shifts with peaks at 284 nm (π→π*) and 342 nm (n→π*), accompanied by an MLCT band at 390 nm and a d-d transition at 580 nm assigned to $^2B1g \rightarrow {}^2A1g$ transition, characteristic of Jahn-Teller distorted octahedral geometry. The Zn(II) and Cd(II) complexes, due to their d^{10} electronic configuration, show only intraligand transitions without any d-d bands. The Zn(II) complex displays bands at 277 nm (π→π*) and 317 nm (n→π*), while the Cd(II) complex shows absorption maxima at 279 nm (π→π*) and 320 nm (n→π*). The bathochromic shifts observed in the π→π* and n→π* transitions of the complexes compared to the free ligand (red shifts of 10-20 nm) provide strong evidence for successful coordination through the azomethine nitrogen and other donor atoms. Additionally, the appearance of new bands in the visible region attributed to charge transfer and d-d transitions further confirms the formation of the metal complexes. The positions and intensities of these bands are consistent with octahedral geometry around the metal centers, with possible distortions in some cases, particularly for the Cu(II) complex due to the Jahn-Teller effect [18-21].

4.4. IR spectral studies

The IR spectrum of Schiff base ligand (L) was carried out in the range of 4000– 400 cm^{-1} and listed in Table 2 (Supplementary Figure S2). The IR vibrational bands of the triazole Schiff base ligand showed a band at 1627 cm^{-1}, which indicated the formation of υ(C=N) of the azomethine group [1, 15]. The NH vibration of pyrrole in the ligand was observed at 3120 cm^{-1}, and the bending band at 1512 cm^{-1}. The weak band at 1055 cm^{-1} was assigned to triazole's N–N vibration [11, 24]. A medium band at 1458 cm^{-1} could be attributed to the stretching vibration of the pyridyl ring of the quinolone [25, 26]. The pyridyl ring's in-plane bending vibration δ(C=N) band was observed at 682 cm^{-1} [27]. Significant shifts in the stretching vibration confirmed the formation of complexes. The band of azomethine vibration was shifted to a higher frequency by 16 – 43 cm^{-1} (from 1643 to 1670 cm^{-1}). The shift in band position ascertained the involvement of azomethine N in chelation. While the band at 1570 $cm^{-1}$of υ(C=N) of quinoline was shifted to a lower frequency by 8–27 cm^{-1} (1562–1543 cm^{-1}) in the IR spectra of metal complexes, indicating the involvement of the quinoline N in the coordination [28, 29]. The in-plane bending vibration δ(C=N) band of the pyridyl ring of the ligand was observed at 620 cm^{-1} and for the complexes at 617–663 cm^{-1}, which further supports the coordination via pyridyl nitrogen [26]. Also, bands assigned to vibration of -NH and N–N groups of triazole moiety remained unchanged at the same range 3110–3120 and 1050–1060 cm^{-1}, showing their non-involvement in complexation [11, 29]. Moreover, the appearance of new weak bands at 420–480 cm^{-1} was assigned to M–N [30]. In the complexes of Ni(II) and Cu(II), bands at 520 and 510 cm^{-1}, respectively, appeared due to the M–O bond [25, 30]. Abroad band from 3305–3433 cm^{-1} due to hydrated or coordinated water molecules. In addition, the bands due to the waging and rocking modes of coordinated water were observed at 968–985 cm^{-1}[24, 31].

Table 2: Characteristic IR bands 400 – 4000 (cm^{-1}) for Schiff base ligand (L) and its complexes.

Compound	$\upsilon(-OH)_{H2O}$	$\upsilon(C=N)_{Azomethine}$	$\upsilon(C=N)_{quinoline}$	υ (M-O)	υ(M-N)
L	-----	1627 m	1570 m	-----	-----
$[Cr(L)_2Cl_2]Cl.4H_2O$	3421 s	1647 s	1546 s	----	478 m
$[Mn(L)_2Cl2].3H_2O$	3371 m	1651 s	1554 s	-----	475 m
$[Fe(L)_2Cl2]Cl.4H_2O$	3390 m	1643 m	1558 m	----	443 m
$[Co(L)_2Cl_2].2H_2O$	3305 w	1647 s	1558 m	----	480 m
$[Ni(L)_2(H_2O)Cl]Cl.H_2O$	3433 w	1647 s	1543 w	520 w	478 w
$[Cu(L)_2(H_2O)Cl]Cl.2H_2O$	3433 w	1647 s	1562 m	510 w	478 w
$[Zn(L)_2Cl_2].3H_2O$	3417 s	1651 s	1550 s	----	475 w
$[Cd(L)_2Cl_2].3H_2O$	3313 w	1670 m	1546 m	----	474 w

Where, b; broad, w; weak, m; medium, s; sharp.

4.5. ^{1}H-NMR Spectral Study

The ^{1}H NMR spectral analysis provided valuable insights into the structure and coordination behavior of the Schiff base ligand (L) and its Zn(II) and Cd(II) complexes (Supplementary Table S1). The spectra were recorded in $(CD_3)_2SO$ (DMSO-d^6) solution, using $(CH_3)_4Si$ (TMS) as an internal standard. In the spectrum of the free ligand, a signal at δ = 8.85 ppm was observed, characteristic of the azomethine group (-CH=N). The aromatic protons of the quinoline ring appeared as multiplets in the range of δ 7.48–8.80 ppm [25]. Upon complexation, the ^{1}H NMR spectra of $[Zn(L)_2Cl_2]\cdot 3H_2O$ and $[Cd(L)_2Cl_2]\cdot 3H_2O$ showed slight downfield shifts of the azomethine proton to δ = 8.84 and 8.83 ppm, respectively. This shift indicates the involvement of the azomethine nitrogen in coordination with the metal ions. The aromatic protons of the quinoline ring experienced an upfield shift, appearing at δ 7.50–8.50 ppm for the Zn(II) complex and δ 6.96–8.70 ppm for the Cd(II) complex. These shifts suggest the coordination of the metal ions via the nitrogen of the pyridine ring in the quinoline moiety [25, 27]. New signals at δ 3.61 ppm and δ 3.34 ppm were observed in the Zn(II) and Cd(II) complexes, respectively, attributed to the presence of hydrated water molecules [15, 27]. The NH proton signal of the free ligand at δ 12.80 ppm remained largely unchanged in both complexes (δ = 12.70 ppm), indicating that this proton is not involved in metal coordination. These spectral changes support the proposed coordination mode of the Schiff base ligand to the metal centers through the azomethine nitrogen and the quinoline Table 3. ^{1}H NMR spectral data for the Schiff base ligand (L) and its Zn(II) and Cd(II) complexes in DMSO-d^6.

4.6. Thermal studies

Thermogravimetric analysis (TGA) was employed to elucidate the thermal behavior of the Schiff base ligand (L) and its corresponding metal complexes over a temperature range of 30–970 °C [1, 20, 21, 32]. The correlation between temperature and mass loss percentage is presented in Table 3 (Supplementary Figure 3). The TG curve of the Schiff base ligand showed two decomposition steps. The first step at the temperature range of 30–375 °C and suite loss of $C_2H_2N_2$ molecule (found at 36.77%, calc. 36.77%), and the second step at the temperature range of 375–850 °C suited to loss of $C_{10}H_7N$ molecule (found 63.21%, calc. 63.23%). The Cr(III) complex decomposed in four steps within the temperature range from 35 to 940 °C. The first step is between 35–125 °C, which indicates the loss of two and a half miles of hydrated water, with a mass loss of 6.55% (calc. 6.35%). The second step is within the temperature range of 125–285 °C, corresponding to the loss of the 2HCl and $C_2H_2N_3$ molecule, with a mass loss of 20.48% (calc. 20.84%). The third step between 285–685 °C was attributed to the loss of HCl and the organic moiety, $C_{10}H_7N_2$, with found mass loss of 27.74% (calc. 28.31%). The fourth step is between 685–940 °C corresponding to the loss of $C_{12}H_9N_5$ molecule, with mass loss of (found 32.79 %, calc. 32.96%), leaving behind the chromium oxide residue with total mass loss amounted to (found 87.56%, calc. 88.76%).

The decomposition of the Mn(II) complex occurred in three steps. The first step is within the temperature range of 25–305 °C and corresponds to the loss of two moles of hydrated water and HCl molecule with mass loss of (found 12.11%, calc. 12.60%). The second decomposition occurred within the 305–560 °C temperature range and was assigned to the loss of HCl and $C_4H_4N_4$ molecule, with found mass losses of 22.77% (calc. 23.12%). The final stage is the loss of the $C_{20}H_{14}N_6$ molecule, between 560–950 °C, with a mass loss of 53.78% (calc. 54.08%). The final residue is manganese oxide, with a total found mass loss of 88.66% (calc. 88.80%). The Fe(III) complex decomposed in four steps within the temperature range from 40 to 970 °C. The first step is between 40–200 °C, which accounted for the loss of two moles of water of hydration, with mass loss of (found 5.18%, calc5.29%). The second step is within the temperature range of 200– 585 °C, corresponding to the loss of 2HCl and $C_{10}H_7N_2$ molecule, with found mass loss of 33.11% (calc. 33.50%). The third step is between 585–800 °C and is attributed to the loss of HCl and the organic molecule $C_2H_3N_3O_{½}$, with 17.29% found mass loss of (calc. 16.68%). The final step is the loss of the $C_{12}H_9N_2$ molecule, between 800–970 °C with mass loss of (found 32.11%, calc. 32.77%), and leaving ferric oxide residue with a total estimated mass loss amounted to 87.69% (calc. 88.24%).

The TG curve of the Co(II) complex revealed three decomposition steps within the temperature range from 40 to 950 °C. The first step corresponded to the loss of one molecule of hydrated water with mass loss of (found 3.41%, calc. 2.95%) between 40–120 °C. The second step is within the temperature range of 120–570 °C and is attributed to the loss of the 2HCl and $C_{10}H_7N_2$ molecules, with a mass loss of 36.52% (cal. 37.32%). The final step is the loss of the $C_{14}H_{11}N_8$ molecule, between 570 – 950 °C with mass losses of (found 46.87%, calc. 47.63%). The remaining residue is cobalt oxide with a total mass loss of 86.80% (calc. 87.09%). The Ni(II) complex decomposed in four steps within the 25 to 955 °C temperature range. The first step is between 25–105 °C, which indicates the loss of one molecule of hydrated water with a found mass loss of 3.10% (calc. 2.95%). The second step is within the temperature range of 105– 470 °C, corresponding to the loss of the 2HCl and $C_{10}H_7N_2$ molecule, with an estimated mass loss of 37.00% (calc. 37.13%). The third step between 470 – 800 °C attributed to the loss of the organic moiety, $C_4H_2N_6$, with mass loss of (found 22.69%, calc. 22.15%). The fourth step is between 800 – 955 °C and corresponds to the loss of the $C_{10}H_7N_2$ molecule, with a mass loss of 25.20 % (calc. 25.24%), leaving behind the nickel oxide residue with total mass loss amounted to (found 87.99%, calc. 78.45%).

The Cu(II) complex was decomposed in four steps. The first step involved the loss of one mole of hydrated water with mass loss of (found 5.46%, calc. 5.68%) between 35–120 °C. The second step is within the temperature range of 120–320 °C and corresponds to the loss of HCl and $C_3H_3N_4$ molecule, with found mass loss of 20.33% (calc. 20.74%). The third step was within the temperature range from 320 to 640 °C, corresponding to the loss of HCl and the organic moiety C_9H_6N, with mass loss of (found 25.82%, calc. 25.95%). The last step within the temperature ranged from 640 to 955 °C, corresponding to the loss of the organic moiety $C_{12}H_{12}N_5$, with found mass loss of 34.80% (calc. 35.17%). Finally, copper oxide remains as residue with a total estimated mass loss of 86.40% (calc. 87.54%). The Zn(II) complex decomposed in three steps within the temperature range from 50 to 950 °C. The first step is between 50–265 °C, which indicates the loss of two moles of water of hydration and HCl, with mass loss of (found 11.52%, calc. 11.40%). The second step is within the temperature range of 265–520 °C, corresponding to the loss of the HCl and $C_3H_3N_4$ molecule, with a mass loss of 20.10% (calc. 20.18%). The third step is between 520–955 °C and is attributed to the loss of the organic moiety $C_{21}H_{15}N_6$, with an estimated mass loss of 54.49% (calc. 55.19%). Finally, the zinc oxide as residue with total mass loss amounting to 86.11% (calc. 87.27%).

The Cd(II) complex decomposed within the 25 to 900 °C temperature range in three steps. The first step is between 25–160 °C, which indicates the loss of two molecules of hydrated water, with mass loss of (found 5.17%, calc. 5.27%). The second step is within the temperature range of 160–420 °C, corresponding to the loss of 2HCl and $C_{10}H_7N_2$ molecule, with mass loss of (found 33.28%, calc. 33.38%). The third step is between 420–900 °C and is attributed to the loss of the organic moiety,

$C_{14}H_{11}N_8$, with a mass loss of (found 41.49%, calc. 42.61%), leaving behind the cadmium oxide residue with a total estimated mass loss amounted to 79.94% (calc. 81.16%).

Table 3: Thermal decomposition steps of (L) and its metal complexes.

Compound	TG range ° C	DTG_{max} °C	n#	Mass loss% found.(calc.)	Total mass loss %found.(Calc.)	Assignment	Metallic residue
L	30 – 375	80, 275	1	36.77 (36.77)	99.98 (100)	Eliminate of $C_2H_2N_4$.	----
	375 – 850	435	1	63.21 (63.23)		Eliminate of $C_{10}H_7N$.	
$[Cr(L)_2Cl_2]Cl.4H_2O$	35 – 125	74	1	6.55 (6.35)	87.56 (88.76)	Loss of 2½H_2O.	½(Cr_2O_3)
	125 – 285	256	1	20.48 (20.84)		Loss of 2HCl +$C_2H_2N_3$.	
	285 – 685	385,484	1	27.74 (28.31)		Loss of HCl +$C_{10}H_7N_2$.	
	685 – 940	777	1	32.79 (32.96)		Loss of $C_{12}H_9N_5$.	
$[Mn(L)_2Cl_2].3H_2O$	25 – 305	84	1	12.11 (11.60)	88.66 (88.80)	Eliminate of 2H_2O + HCl.	MnO
	305 – 560	199	1	22.77 (23.12)		Loss of HCl + $C_4H_4N_4$.	
	560 – 900	548	1	53.78 954.08)		Eliminate of $C_{20}H_{14}N_6$.	
$[Fe(L)_2Cl_2]Cl.4H_2O$	40 – 200	89	1	5.18 (5.29)	87.69 (88.24)	Loss of 2H_2O.	½(Fe_2O_3)
	200 – 585	235	1	33.11 (33.50)		Loss of 2HCl + $C_{10}H_7N_2$.	
	585 – 800	598, 793	1	17.29 (16.68)		Loss of HCl + $C_2H_3N_3O_{1/2}$.	
	800 – 970	840	1	32.11 (32.77)		Loss of $C_{12}H_9N_2$.	
$[Co(L)_2Cl_2].2H_2O$	40 – 120	73	1	3.41 (2.95)	86.80 (87.90)	Loss of H_2O.	CoO
	120 – 570	172, 277	1	36.52 (37.32)		Loss of 2HCl + $C_{10}H_7N_2$.	
	570– 950	696	1	46.87 (47.63)		Loss of $C_{14}H_{11}N_8$.	
$[Ni(L)_2(H_2O)Cl]Cl.H_2O$	25 – 150	73	1	3.10 (2.93)	87.99 (87.45)	Loss of H_2O.	NiO
	105 – 470	195, 447	1	37.00 (37.13)		Loss of 2HCl +$C_{10}H_7N_2$.	
	470 – 800	487	1	22.69 (22.15)		Loss of $C_4H_2N_6$.	
	800 – 955	870	1	25.20 (25.24)		Loss of $C_{10}H_7N_2$.	
$[Cu(L)_2(H_2O)Cl]Cl.2H_2O$	35 – 120	81	1	5.46 (5.68)	86.40 (87.54)	Loss of 2H_2O.	CuO
	120 – 320	166, 219	1	20.33 (20.74)		Loss of HCl + $C_3H_3N_4$.	
	320 – 640	330	1	25.82 (25.95)		Loss of HCl + C_9H_6N.	
	640 – 955	652	1	34.80 (35.17)		Loss of $C_{12}H_{12}N_5$.	
$[Zn(L)_2Cl_2].3H_2O$	50 – 265	112, 162	1	11.52 (11.40)	86.11 (87.27)	Loss of 2H_2O + HCl.	ZnO
	265 – 520	315, 400	1	20.10 (20.18)		Loss of HCl + $C_3H_3N_4$.	
	520 – 955	592	1	54.49 (55.19)		Loss of $C_{21}H_{15}N_6$.	
$[Cd(L)_2Cl_2].3H_2O$	25 – 160	78, 128	1	5.17 (5.27)	79.94 (81.16)	Loss of 2H_2O.	CdO
	160 – 420	267, 394	1	33.28 (33.38)		Loss of 2HCl + $C_{10}H_7N_2$.	
	420 – 900	507	1	41.49 (42.61)		Loss of $C_{14}H_{11}N_8$.	

4.7. UV-Visible Absorption Studies

The UV-visible absorption analysis provided valuable insights into the electronic structures of the free Schiff base ligand (L) and its corresponding metal complexes. These spectra were obtained using dimethylformamide (DMF) as the solvent, with measurements taken at room temperature across a wavelength range of 200-700 nm. Pure DMF served as the reference for these measurements. The free ligand (L) spectrum examination revealed two distinct absorption bands. The first band, observed at 266 nm, was attributed to π–π* transitions within the molecule's conjugated system. The second band, appearing at 316 nm, was associated with n–π* transitions, typically involving non-bonding electrons on heteroatoms such as nitrogen. Significant changes were observed in the UV-visible spectra upon the formation of metal complexes. The π–π* transition band experienced a bathochromic shift, moving to longer wavelengths in the range of 276-286 nm for the various metal complexes. Similarly, the n–π* transition band also underwent a redshift, appearing in the complexes' 317-348 nm range. These spectral shifts, along with changes in absorption intensity, can be attributed to the chelation effect. The coordination of the ligand to the metal centers enhances the overall conjugation and electron delocalization within the molecular system. This increased conjugation alters the energy levels of the π and π* orbitals, as well as the non-bonding orbitals, resulting in the observed changes in the π–π* and n–π* transitions of the conjugated chromophores. The bathochromic shifts and intensity changes in the absorption bands provide evidence for the successful formation of metal complexes and provide insights into the electronic structure of these coordination compounds [20, 21]. These observations highlight the significant impact of metal coordination on the ligand's electronic properties.

4.8. Molecular Modeling

4.8.1. Geometrical Optimization

The molecular modeling studies, employing Density Functional Theory (DFT) calculations with the B3LYP functional and the 6-311G(d,p) basis set for non-metal atoms and LANL2DZ for transition metals, provided comprehensive insights into the electronic and structural properties of the Schiff base ligand (L) and its Cu(II) and Fe(III) complexes [1, 20, 21, 33, 34]. The optimized geometries revealed significant distortions in bond angles and lengths upon metal complexation, leading to distorted octahedral structures for both metal complexes (Fig 1). For the $[Cu(L)_2(H_2O)Cl]Cl\cdot 2H_2O$ complex, the calculations indicated a distorted octahedral geometry around the Cu(II) center. This distortion is consistent with the Jahn-Teller effect commonly observed in Cu(II) complexes, which typically leads to elongation along one axis of the octahedron. Similarly, the $[Fe(L)_2Cl_2]Cl\cdot 4H_2O$ complex exhibited deviations from ideal octahedral geometry, likely due to the steric demands of the bulky Schiff base ligands and the presence of coordinated water molecules. The bond length and angles are illustrated in the supplementary table S1, which indicates the distortion in the ideal octahedral of metal complexes.

The electronic parameters calculated for these structures provided further insight into their properties using equations (1-8) [33].

$$\Delta E = E_{LUMO} - E_{HOMO} \quad \text{Eq. (1)}$$

$$\chi = \frac{-(E_{HOMO}+E_{LUMO})}{2} \quad \text{Eq. (2)}$$

$$\eta = \frac{E_{LUMO}-E_{HOMO}}{2} \quad \text{Eq. (3)}$$

$$\sigma = \frac{1}{\eta} \quad \text{Eq. (4)}$$

$$Pi = -\chi \quad \text{Eq. (5)}$$

$$S = \frac{1}{2\eta} \quad \text{Eq. (6)}$$

$$\omega = \frac{Pi^2}{2\eta} \quad \text{Eq. (7)}$$

$$\Delta N_{max} = -\frac{Pi}{\eta} \quad \text{Eq. (8)}$$

The HOMO-LUMO energy gap for the ligand was 2.707 eV, decreasing significantly to 0.6 eV for the Cu(II) complex and 0.695 eV for the Fe(III) complex (Table 4). This narrowing of the energy gap upon complexation indicates increased reactivity of the metal complexes. The electrophilicity index (ω) dramatically increased from 5.476 eV for the ligand to 51.39 eV for the Cu(II) complex and 36.985 eV for the Fe(III) complex, reflecting the enhanced electron-accepting ability of the metal centers. The absolute hardness (η) decreased from 1.3535 eV for the ligand to 0.30 eV and 0.3475 eV for the Cu(II) and Fe(III) complexes, respectively, while the absolute softness (σ) increased correspondingly. This trend suggests higher polarizability and potential reactivity of the metal complexes compared to the free ligand [1, 20]. The chemical potential (Pi) became more negative, from -3.850 eV for the ligand to -5.253 eV and -5.070 eV for the Cu (II) and Fe(III) complexes, respectively, indicating a greater tendency to lose electrons in the complexes. The dipole moments also increased significantly upon complexation, from 3.02 Debye for the ligand to 5.1429 Debye for the Cu(II) complex and 8.021 Debye for the Fe(III) complex, reflecting the asymmetric charge distribution in the distorted octahedral structures. The total energy calculations show the stability of the complexes, with the Cu(II) complex at -3649.86 a.u. and the Fe(III) complex at -3455.160 a.u (Table 4). These computational results, accounting for the structural distortions and changes in electronic parameters, provide a comprehensive theoretical foundation for understanding the complex interplay between geometric and electronic factors in these Schiff base metal complexes (Fig 1). The observed changes from the free ligand to the metal complexes highlight the significant impact of coordination on these systems' electronic properties and reactivity.

Table 4: Quantum chemical Pparameters of (L) and its Co(II) and Cu(II) complexes.

Compounds	E_{HOMO} (ev)	E_{LUMO} (ev)	ΔE (ev)	χ (ev)	η (ev)	σ (ev)	Pi (ev)	S (ev^{-1})	ω (ev)	ΔN_{max} (ev)	Total energy (a.u.)	Dipole Moment (Depy)
L	-5.204	-2.497	2.707	3.850	1.3535	0.7388	-3.850	0.3694	5.476	2.844	-736.279	3.02
$Cu(L)_2(H_2O)Cl]Cl.2H_2O$	-5.553	-4.953	0.6	5.253	0.30	3.333	-5.253	1.666	51.39	18.51	-3649.86	5.1429
$Fe(L)_2Cl_2]Cl.4H_2O$	-5.418	-4.723	0.695	5.070	0.3475	2.877	-5.070	1.4388	36.985	14.5895	-3455.160	8.021

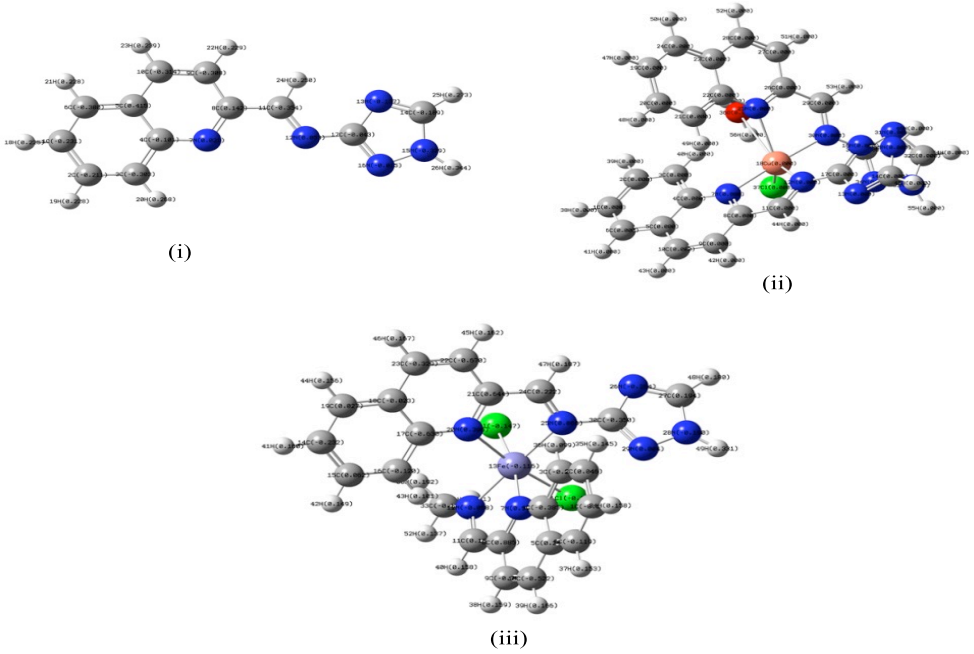

Fig. 1. The optimization compounds where, i) the Schiff base ligand (L), (ii) Cu(II) complex and (iii) Fe(III) complex.

4.9. Biological activity

The in vitro biological activity of the synthesized Schiff base ligand (L) and its metal complexes was evaluated against various microorganisms, including both bacteria and fungi. As shown in Table 5, The study encompassed four bacterial strains - two Gram-positive (*Staphylococcus aureus* and *Streptococcus mutans*) and two Gram-negative (*Escherichia coli* and *Klebsiella pneumonia*) - as well as two fungal species (*Candida albicans* and *Asperagillus nigar*) [1, 20]. Antibacterial Activity: The results revealed a complex pattern of antimicrobial efficacy across the tested compounds. Notably, the free ligand (L) demonstrated moderate to strong activity against all bacterial strains, with inhibition zones ranging from 12.3 mm to 15.0 mm. Among the metal complexes, the $[Cr(L)_2Cl_2]Cl{\cdot}4H_2O$ complex showed the broadest spectrum of activity, inhibiting all tested bacterial strains with zones ranging from 11.4 mm to 17.2 mm. The $[Co(L)_2Cl_2]{\cdot}2H_2O$ complex also exhibited significant activity against most strains, with inhibition zones up to 17.3 mm for *E. coli*. Interestingly, some complexes showed selective activity. For instance, the $[Fe(L)_2Cl_2]Cl{\cdot}4H_2O$ complex was effective against Gram-negative bacteria (11.0 mm for *E. coli* and 18.0 mm for K. pneumonia) but showed no activity against Gram-positive strains. The $[Cu(L)_2(H_2O)Cl]Cl{\cdot}2H_2O$ and $[Zn(L)_2Cl_2]{\cdot}3H_2O$ complexes demonstrated broad-spectrum activity, albeit with generally smaller inhibition zones compared to the free ligand. The $[Cd(L)_2Cl_2]{\cdot}3H_2O$ complex stood out with exceptional activity against Gram-positive bacteria, showing the largest inhibition zones of 28.3 mm against *S. mutans* and 21.3 mm against *S. aureus*, surpassing even the standard antibiotic ampicillin. Antifungal Activity: The antifungal screening revealed that none of the tested compounds, including the free ligand and metal complexes, showed any activity against *Asperagillus nigar*. However, several compounds demonstrated activity against *Candida albicans*. The free ligand showed moderate activity with an inhibition zone of 12.2 mm. Among the metal complexes, $[Cr(L)_2Cl_2]Cl{\cdot}4H_2O$ exhibited the highest antifungal activity against *C. albicans* with an inhibition zone of 13.5 mm, slightly surpassing the free ligand. The $[Co(L)_2Cl_2]{\cdot}2H_2O$, $[Zn(L)_2Cl_2]{\cdot}3H_2O$, and $[Cu(L)_2(H_2O)Cl]Cl{\cdot}2H_2O$ complexes also showed notable activity against *C. albicans*, with inhibition zones ranging from 10.4 mm to 11.6 mm. It's important to note that while some metal complexes showed enhanced activity compared to the free ligand in certain cases, the overall trend indicated that complexation often resulted in reduced antimicrobial efficacy. This observation suggests that the antimicrobial activity is not solely dependent on the presence of metal ions but is influenced by a synergistic effect of various factors, including cell permeation, solubility, dipole moment, and conductivity, all of which are affected by metal complexation [35-37]. In conclusion, this study highlights the potential of these Schiff base compounds and their metal complexes as antimicrobial agents, with particular promise shown by the cadmium complex against Gram-positive bacteria. However, further research is needed to fully understand the structure-activity relationships and the mechanisms underlying their biological activity.

Table 5: Antimicrobial inhibition zones (mm) of Schiff base ligand (L) and its metal complexes.

Compound	Inhibition zone diameter (mm mg^{-1})					
	Antibacterial				Anti-fungi	
	Gram (+)		Gram (-)			
	Staphylococcus aureus	***Streptococcus mutans***	***Klebsiella pneumonia***	***Escherichia coli***	***Candida albicans***	***Asperagillus Nigar***
L	18.1±1.0	16.2±1.0	19.1±0.6	19.0±1.0	16.2±1.0	**NA**
$[Cr(L)_2Cl_2]Cl.4H_2O$	12.3±0.6	13.2±1.0	14.5±1.6	15.0±1.0	12.2±1.0	**NA**
$[Mn(L)_2Cl_2].3H_2O$	11.4±1.0	11.6±0.6	17.2±1.0	16.8±1.0	13.5±1.0	**NA**
$[Fe(L)_2Cl_2]Cl.4H_2O$	NA	NA	15.3±0.6	NA	NA	**NA**
$[Co(L)_2Cl_2].2H_2O$	NA	NA	18.0±1.0	11.0±1.0	9.3±0.6	**NA**
$[Ni(L)_2(H_2O)Cl]Cl.H_2O$	10.7±0.6	15.0±1.0	17.1±0.6	17.3±0.6	11.6±0.6	**NA**
$[Cu(L)_2(H_2O)Cl]Cl.2H_2O$	9.3±0.6	NA	11.0±1.0	NA	NA	**NA**
$[Zn(L)_2Cl_2].3H_2O$	13.3±0.6	13.0±1.0	15.0±1.0	15.7±0.6	10.4±1.0	**NA**
$[Cd(L)_2Cl_2].3H_2O$	14.3±0.6	12.7±1.0	16.3±1.0	16.0±0.6	11.2±0.6	**NA**
Ampicillin	21.3±0.6	28.3±0.6	---	---	---	**---**
Getamicin	---	---	27.0±1.0	25.3±0.6	---	**---**
Amphotericin B	---	---	---	---	21.7±0.6	**19.3±0.6**
DMSO	**---**	**----**	**----**	**----**	**----**	**----**

NA; no activity

The antimicrobial activity results demonstrate that metal complexation significantly enhances the biological efficacy compared to the free Schiff base ligands. This enhancement can be attributed to the chelation theory, wherein coordination of the Schiff base with metal ions creates complexes with both polar and nonpolar properties, facilitating their penetration through cellular membranes [18-21]. The decreased polarity of the metal ion, resulting from orbital overlap during chelation and charge distribution among donor groups, promotes π-electron delocalization across the chelate ring, thereby enhancing membrane permeability [38, 39]. Comparing our findings with recent work by Mansour et al. (2024) [1] who studied quinazoline Schiff base complexes, several interesting parallels emerge. In their study, the Cd(II) complex showed remarkable activity with inhibition zones of 28.3 mm against *S. mutans* and 21.3 mm against *S. aureus*, which closely aligns with our results where our Cd(II) complex demonstrated similar potent activity. This consistency in Cd(II) complex efficacy across both studies suggests the particular effectiveness of cadmium-based complexes against Gram-positive bacteria. Our Cu(II) complex showed inhibition zones of 15.7 mm against *E. coli* and 13.3 mm against *S. aureus*, which is comparable to their Cu(II) complex that exhibited zones of 12.0 mm against *E. coli* and 23.3 mm against *S. aureus*. The slight variations in activity could be attributed to the different structural features of the ligands used, though both studies confirm the significant antimicrobial potential of copper complexes. Interestingly, both studies observed that the Co(II) complexes showed selective activity. In their work, the Co(II) complex demonstrated notable activity against *S. aureus* (19.0 mm) while showing no activity against certain strains, which parallels our findings where Co(II) complexes showed varied effectiveness against different bacterial species. The antifungal results also show similarities, particularly against *C. albicans*, where both studies demonstrated significant activity of the metal complexes. Their Cd(II) complex showed superior antifungal activity, which aligns with our observations of enhanced antifungal properties in cadmium-based complexes. The mechanism of action appears to be similar in both studies, with the effectiveness against microbes being influenced by several crucial elements, including the metal ion's characteristics, ligand properties, coordination sites, complex geometry, concentration, hydrophobicity, and presence of co-ligands. Both studies suggest that if the geometric and charge distribution around a substance does not match the configuration within the bacterial

cell wall pores, it cannot penetrate the wall, compromising its compatibility and preventing toxic reactions inside the pores. These parallel findings across both studies strengthen the understanding of structure-activity relationships in metal-based antimicrobial agents and provide valuable insights for the future design of more effective antimicrobial compounds. The consistent performance of certain metal complexes, particularly those containing Cd(II) and Cu(II), suggests promising directions for further development of metal-based antimicrobial agents.

4.10. Molecular docking study

The molecular docking study provides valuable insights into the potential interactions between the triazole Schiff base ligand (L) and various protein receptors. This computational approach aims to simulate the molecular recognition process, optimizing the conformation of both the ligand and the protein to minimize the free energy of the overall system [1, 34]. Figures 2 and 3 illustrate the acceptable interactions between the Schiff base ligand (L) and the receptors of each protein. At the same time, Table 6 summarizes the energy values obtained from the docking calculations of the free ligand with these receptors. The docking processes revealed several key observations regarding the underlying mechanism of action. The ligation mode primarily focused on the nitrogen atom, the 5-membered ring, and the 6-membered ring sites of the ligand. The main binding receptor backbones were identified as asparagine, glutamate, and alanine residues. The interactions encompassed a variety of types, including π-H, π-π, hydrogen donor, and hydrogen acceptor bonds. The docking results indicated varying degrees of binding affinity for different protein receptors. *Neisseria gonorrhoeae* (5WAQ) showed the highest binding energy value of -7.4 kcal mol^{-1}, with interactions occurring through hydrogen donor bonding. *Staphylococcus aureus* (1GHP) exhibited a binding energy of -4.7 kcal mol^{-1}, involving hydrogen donor bonding. *Staphylococcus mutans* (2ZIC) and receptor 7DAE demonstrated binding energies of -4.2 kcal mol^{-1}, with interactions primarily through π-H bonding and hydrogen acceptor bonding, respectively. Based on these results, the receptor of *Neisseria gonorrhoeae* (5WAQ) demonstrated the most favorable interaction with the Schiff base ligand (L) compared to the other receptors studied. This finding suggests that the ligand may have a powerful potential for targeting this bacterial species. These molecular docking results provide a theoretical foundation for understanding the potential antimicrobial activity of the Schiff base ligand. They offer insights into the possible mechanisms of action and highlight the importance of specific structural features in determining the ligand's affinity for different bacterial targets. However, it's important to note that while these computational results are promising, they should be corroborated with experimental studies to validate the predicted interactions and their biological significance fully.

Table 6: Energy values obtained in docking calculations of Schiff base ligand L with receptors of crystal structure cell cancer (7DAE), COVID-19 (6W41), *Candida alibican* (5JPE), *Neisseria gonorrhoeae* (5WAM and 5WAQ), *Pseudomonas aeruginosa* (3ix3), *Bacillus subtilis* (3AHU), *Staphylococcus aureus* (1GHP, 1JIJ and 1JIL) and *Staphylococcus mutans* (2ZIC and 3AIC).

Receptor	Ligand moiety	Receptor site	Interaction	Distance (A°)	E (k cal mol^{-1})
7DAE	N 15	OD1 ASP 69 (A)	H-donor	3.25	-3.9
	N 16	N GLN 11 (A)	H-acceptor	3.00	-4.3
6W41	5-ring	CA ALA 344 (C)	pi-H	4.02	-1.6
5JPE	N 7	ND2 ASN 289 (A)	H-acceptor	3.70	-0.8
	6-ring	CE1 HIS 231 (A)	pi-H	4.77	-0.6
	5-ring	OH TYR 299 (A)	pi-H	4.02	-0.9
	6-ring	OH TYR 437 (A)	pi-H	3.90	-0.7
	6-ring	OH TYR 437 (A)	pi-H	4.67	-0.6
3IX3	5-ring	OH TYR 56 (A)	pi-H	3.82	-3.0
1GHP	N 15	O ASP 272 (A)	H-donor	3.01	-4.7
1JIJ	N 16	N GLY 193 (A)	H-acceptor	3.06	-4.0
1JIL	6-ring	N GLY 193 (A)	H-acceptor	3.49	-1.6
3AHU	N 15	O PHE 62 (A)	H-donor	3.17	-3.4
	N 16	N PHE 62 (A)	H-acceptor	3.27	-3.1
2ZIC	N 15	SD MET 1 (A)	H-donor	3.27	-4.2
3AIC	N 15	OD1 ASP 909 (A)	H-donor	2.95	-0.7
	N 13	NE2 HIS 587 (A)	H-acceptor	3.25	-3.7
5WAM	6-ring	CA GLY 61 (A)	pi-H	4.37	-0.7
	5-ring	N THR 77 (A)	pi-H	3.70	-3.7
5WAQ	N 15	OD1 ASP 109 (A)	H-donor	3.10	-7.8
	5-ring	CE2 TYR 162 (A)	pi-H	4.39	-0.7

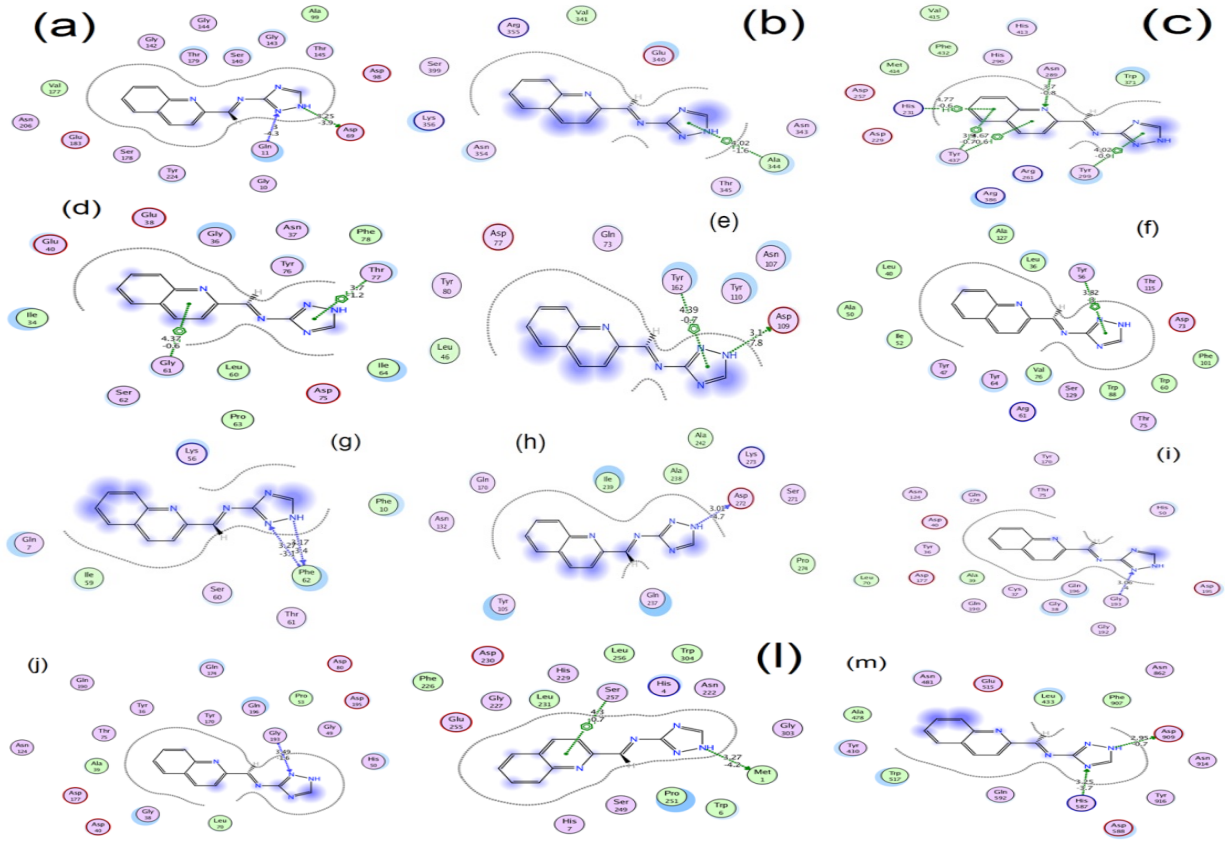

Fig. 2. 2d interaction between the Schiff base ligand L with receptors of crystal structure while; (a) cell cancer (7DAE), (b) COVID 19 (6W41), (c) *Candida alibican* (5JPE), (d, e) *Neisseria gonorrhoeae* (5WAM and 5WAQ), (f) *Pseudomonas aeruginosa* (3ix3), (g) *Bacillus subtilis* (3AHU), (h, i, j) *Staphylococcus aureus* (1GHP, 1JIJ and 1JIL) and (l, m) *Staphylococcus mutans* (2ZIC and 3AIC).

5. Textural Characteristics of Metal Complexes: SEM and AFM Analysis

5.1. The Textural Characteristics of the Complexes

The morphological and textural properties of the synthesized Cu(II) and Fe(III) Schiff base complexes $[Cu(L)_2(H_2O)Cl]Cl{\cdot}2H_2O$ and $[Fe(L)_2Cl_2]Cl{\cdot}4H_2O$ were thoroughly investigated using scanning electron microscopy (SEM) and atomic force microscopy (AFM), as shown in Figure 4 [38, 39]. For the Cu(II) complex, the SEM micrograph reveals a collection of small, uniformly sized particles with a roughly spherical morphology. These nanoparticles exhibit an average diameter of approximately 30 nm, firmly establishing their nanoscale nature. The particles appear well-dispersed, with minimal agglomeration, indicating a successful synthesis process resulting in discrete nanostructures. The AFM images of the Cu(II) complex corroborate these observations, showing a uniform distribution of small, rounded features across the surface in both 2D and 3D representations. The height scale in the AFM images confirms the nanoparticles' dimensions in the range of 30 nm. In contrast, the Fe(III) complex exhibits a distinctly different morphology. The SEM micrograph of the Fe(III) complex shows larger, irregularly shaped structures with a rougher surface texture. These structures appear composed of smaller particles that have coalesced or grown together, resulting in a more complex surface topology. The AFM images of the Fe(III) complex further emphasize this difference. The 2D and 3D AFM maps reveal a more rugged surface topography with larger, irregular structures. The color scale in the AFM images indicates a wider range of heights for the Fe(III) complex compared to the Cu(II) complex, suggesting a more diverse and complex surface structure. The striking difference in morphology between the Cu(II) and Fe(III) complexes may be attributed to several factors, including the distinct coordination environments of the Cu(II) and Fe(III) ions, differences in the crystallization or precipitation processes during synthesis, and potential variations in the interaction between the metal ions and the Schiff base ligands. The Cu(II) complex forms well-defined nanoparticles with high uniformity, which could be advantageous for applications requiring high surface area and consistent properties. On the other hand, the more complex surface structure of the Fe(III) complex might offer interesting properties for catalysis or adsorption

applications due to its increased surface roughness and potential for diverse binding sites. These microscopic studies provide valuable structural information that complements the spectroscopic and computational analyses, contributing to a thorough characterization of the synthesized Schiff base metal complexes. The observed differences in particle size, shape, and surface features between the Cu(II) and Fe(III) complexes may have significant implications for their reactivity, catalytic activity, and potential applications in various materials science and nanotechnology fields [40, 41].

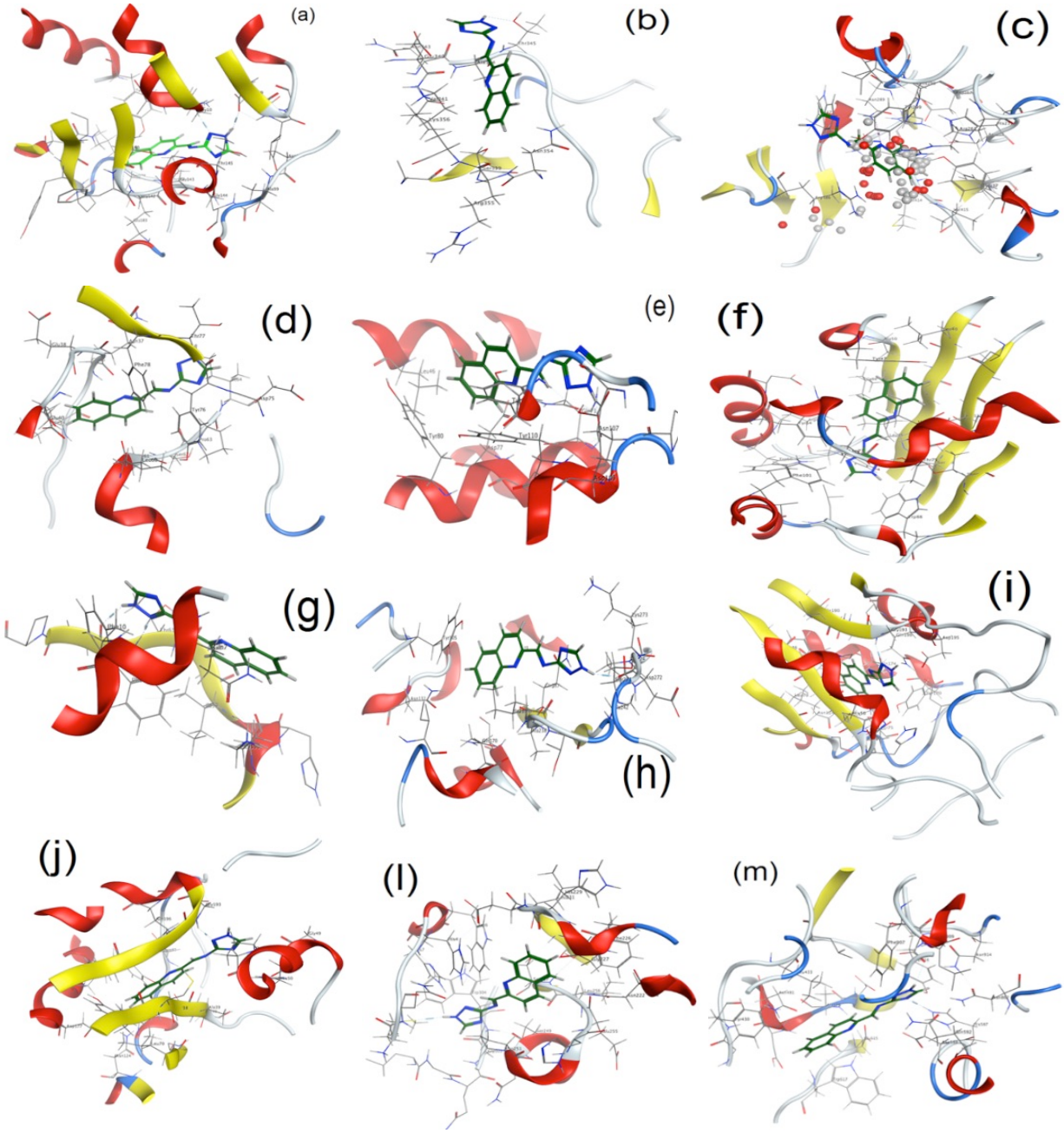

Fig. 3. 3d interaction between the Schiff base ligand L with receptors of crystal structure while; (a) cell cancer (7DAE), (b) COVID 19 (6W41), (c) *Candida alibican* (5JPE), (d, e) *Neisseria gonorrhoeae* (5WAM and 5WAQ), (f) *Pseudomonas aeruginosa* (3ix3), (g) *Bacillus subtilis* (3AHU), (h,i,j) *Staphylococcus aureus* (1GHP, 1JIJ and 1JIL) and (l, m) *Staphylococcus mutans* (2ZIC and 3AIC).

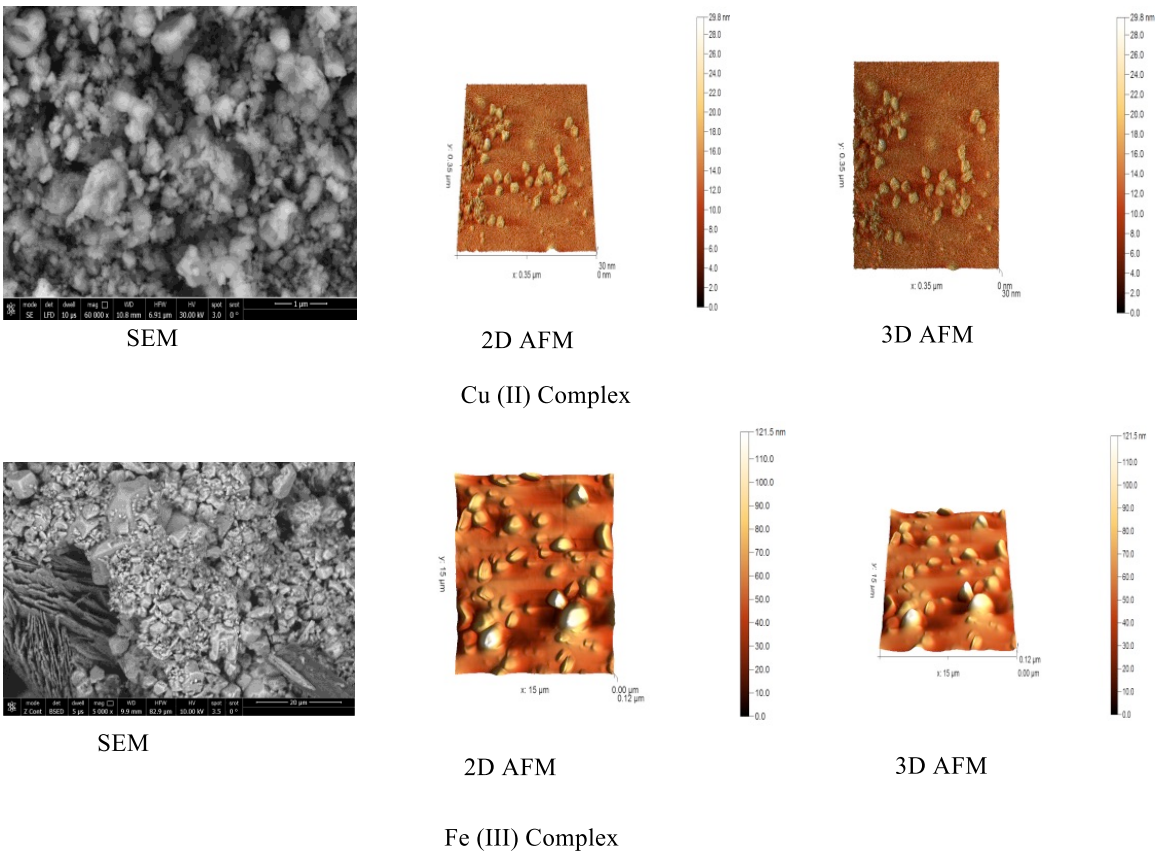

Fig. 4. SEM and AFM images of Cu(II) and Fe(III) complexes, respectively.

5.2. Measurement of BET Surface Area and Pore Size

The Brunauer, Emmett, and Teller (BET) method, a widely adopted technique for the characterization of nanoscale materials, was employed to analyze the surface area and pore characteristics of the synthesized Cu(II) and Fe(III) Schiff base complexes. This approach, which relies on the principle of gas adsorption onto solid surfaces, offers significant efficiency, speed, and user-friendliness advantages for determining surface area in nanostructures [42]. The present study utilized BET adsorption isotherms to evaluate the surface area characteristics of the nano Cu(II) and Fe(III) complex samples. Quantitative analysis of the BET measurements revealed significant differences between the Cu(II) and Fe(III) complexes regarding their surface area and pore characteristics (Fig 5). The Cu(II) complex demonstrated a multipoint BET surface area of 33.4786 m^2/g, indicative of a moderately accessible surface for potential interactions or catalytic activities. This complex's BJH adsorption cumulative pore volume was also determined to be 0.0491931 cc/g, suggesting a notable internal structure capable of accommodating guest molecules or facilitating mass transport processes. The average pore size was calculated to be 3.27499 nm, indicating the presence of mesopores in the structure. In contrast, the Fe(III) complex exhibited a higher multipoint BET surface area of 46.8261 m^2/g, suggesting a more accessible surface than the Cu(II) complex. The BJH adsorption cumulative pore volume for the Fe(III) complex was 0.124864 cc/g, significantly higher than that of the Cu(II) complex. This indicates a more developed porous structure in the Fe(III) complex. The average pore size for the Fe(III) complex was 7.7642 nm, which is considerably larger than that of the Cu(II) complex, suggesting the presence of larger mesopores or even small macropores. Both complexes exhibited type IV nitrogen adsorption-desorption isotherms accompanied by a hysteresis loop, confirming their mesoporous nature. This observation provides valuable insights into the structural properties of the synthesized materials and their potential applications in various fields. The hysteresis loops observed in both isotherms indicate the presence

of ink-bottle-shaped pores, which can be advantageous for certain applications, such as controlled release of adsorbed species. The substantial multipoint BET surface areas observed for both metal complex nanoparticles are particularly interesting, as they significantly enhance the materials' capacity to adsorb harmful contaminants from aqueous solutions. This property renders these complexes potentially valuable for environmental remediation applications, such as water purification or removing toxic substances from industrial effluents. The mesoporous nature of the complexes, as evidenced by the type IV isotherms, further supports their potential efficacy in such applications by facilitating the rapid diffusion of adsorbate molecules throughout the porous structure. The Fe(III) complex, with its higher surface area and larger pore volume, may be particularly effective in applications requiring high adsorption capacity or rapid mass transport. On the other hand, the Cu(II) complex, with its smaller pore size, might be more suitable for applications requiring size-selective adsorption or catalysis [43]. The high surface area and well-defined pore characteristics observed in these metal complexes underscore their potential utility in various applications beyond their primary coordination chemistry interests, including catalysis, gas storage, and selective molecular separations. The distinct differences in surface area and pore characteristics between the Cu(II) and Fe(III) complexes also highlight the influence of the metal center on the overall structural properties of these Schiff base complexes, providing valuable insights for designing tailored materials for specific applications.

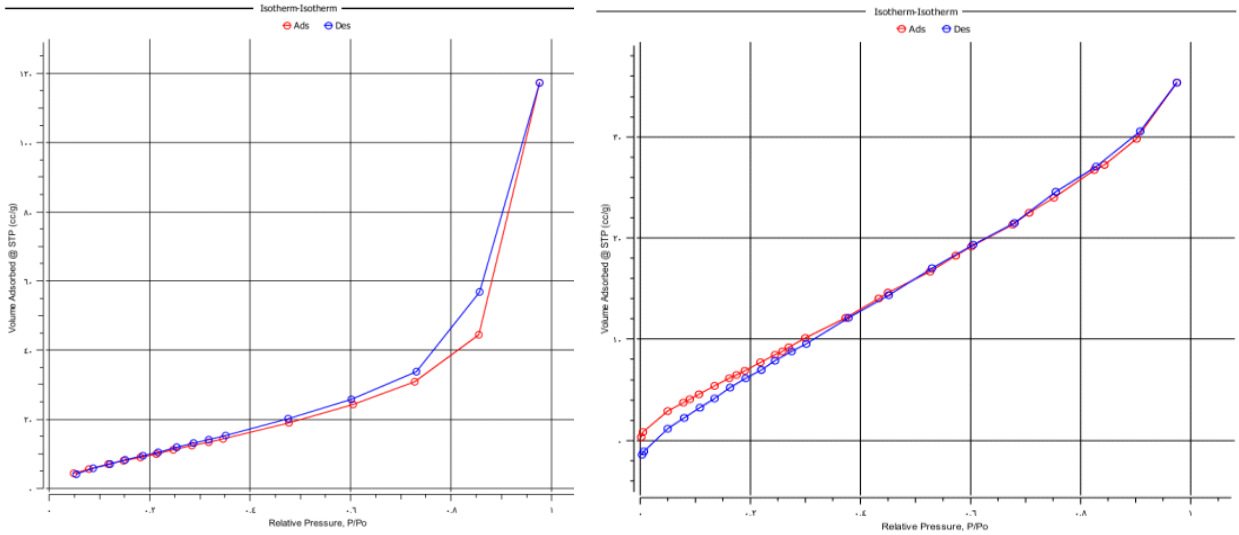

Cu (II) Complex Fe (III) Complex

Fig. 5. BET adsorption isotherms and pore characteristics of Cu(II) and Fe(III) Schiff base complexes.

5.3. Contact Angle Measurement

The wettability and surface energy characteristics of the synthesized Cu(II) and Fe(III) Schiff base complex nanoparticles were evaluated through contact angle measurements. This technique quantifies the angle formed at the interface between a liquid droplet and a solid surface, providing crucial insights into the hydrophobicity or hydrophilicity of materials. These properties significantly influence the behavior of materials in various applications, particularly in aqueous environments [38-41]. As shown in Figure 6, the water contact angles were measured for both the Cu(II) and Fe(III) complex nanoparticles, revealing distinct surface properties for each material. The Cu(II) complex nanoparticles exhibited a water contact angle of 89.012°, indicating a slightly hydrophilic nature. This contact angle, just below 90°, suggests that water droplets slightly tend to spread on the surface of these nanoparticles rather than beading up completely. This property indicates that the Cu(II) complex nanoparticles have a moderate affinity for water. In contrast, the Fe(III) complex nanoparticles demonstrated more hydrophobic characteristics, with a water contact angle of 98.89°. This angle, being greater than 90°, indicates that water droplets tend to bead up more on the surface of these nanoparticles, minimizing the contact area between the water and the particle surface. The observed difference in wettability between the Cu(II) and Fe(III) complex nanoparticles has significant implications for their potential applications, particularly in aqueous media. The slightly hydrophilic nature of the Cu(II) complex could enhance its dispersibility in aqueous solutions, potentially making it more suitable for applications requiring good interaction with water, such as certain catalytic processes or biological systems. On the other hand, the more hydrophobic character of the Fe(III) complex nanoparticles could be advantageous in applications where water repellency is desired, such as in developing water-

resistant coatings or selective extraction processes. The difference in contact angles between the Cu(II) and Fe(III) complexes (89.012° and 98.89°, respectively) suggests that the choice of metal center significantly influences the surface properties of the resulting nanoparticles. This variation could be attributed to differences in the two complexes' coordination environment, crystal packing, or surface morphology. The ability to tune the wettability of these nanoparticles through metal selection or synthetic modifications provides a valuable tool for tailoring their properties for specific applications. These findings contribute to a more comprehensive understanding of the physicochemical properties of the synthesized metal complexes. The distinct wettability characteristics of the Cu(II) and Fe(III) complexes open up new avenues for their application in fields ranging from materials science to environmental remediation and catalysis. For instance, the Cu(II) complex might be more suitable for applications requiring good dispersion in aqueous media. In contrast, the Fe(III) complex could be better suited for applications involving hydrophobic interactions or water-repellent surfaces.

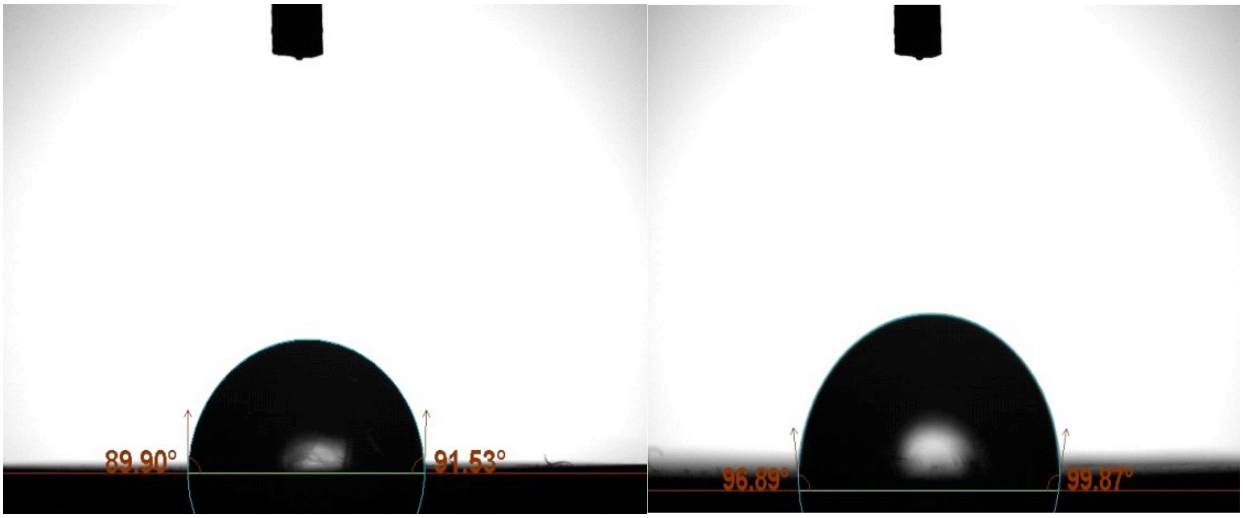

Fig. 6. Contact angle measurements of Cu(II) and Fe(III) Schiff base complex nanoparticles

5.4. Cyclic Voltammetry Analysis and Application of Nanocomplex for Arsenic Detection

5.1. Cyclic Voltammetry

The cyclic voltammograms presented in Figure 7 offer valuable insights into the electrochemical behavior of arsenic species on the Cu(II) and Fe(III) nanocomplex-modified electrodes. These voltammograms demonstrate the effectiveness of both metal complexes in detecting and quantifying arsenic, albeit with some notable differences in their electrochemical responses. For the Cu(II) nanocomplex-modified electrode, the cyclic voltammograms reveal a well-defined anodic peak at approximately 0.2 V, corresponding to arsenite oxidation to arsenate. This peak shows a clear concentration-dependent response, with the current intensity increasing as the arsenic concentration rises from 10 ppm to 25 ppm. The Cu(II) complex also exhibits a cathodic peak around -0.3 V, likely associated with reducing arsenate back to arsenite. The symmetry and reversibility of these peaks suggest a relatively facile electron transfer process at the Cu(II) complex surface. In contrast, the Fe(III) nanocomplex-modified electrode displays a slightly different electrochemical profile. The anodic peak for the Fe(III) complex appears to be shifted to a slightly higher potential, occurring at around 0.25 V. This shift might be attributed to the different coordination environment and redox properties of the Fe(III) center compared to Cu(II). The Fe(III) complex also shows a concentration-dependent response, with peak currents increasing with arsenic concentration. However, the cathodic peak for the Fe(III) complex is less pronounced compared to the Cu(II) complex, suggesting a more irreversible redox process for arsenic species on the Fe(III) surface. The Cu(II) and Fe(III) nanocomplex-modified electrodes demonstrate excellent sensitivity to arsenic concentration changes in the 10 to 25 ppm range. The linear increase in peak currents with concentration for both complexes indicates their potential for quantitative arsenic determination. The baseline currents for both complexes show a slight increase with concentration, particularly in the positive potential region, which may be attributed to capacitive effects or background processes at the electrode surfaces. The distinct electrochemical behaviors of the Cu(II) and Fe(III) nanocomplexes highlight the influence of the metal center on the sensing properties. The Cu(II) complex appears to facilitate a more reversible redox process for arsenic species, which could be advantageous for sensing applications requiring repeated measurements or continuous monitoring. On the other hand, the Fe(III) complex's shifted oxidation potential might offer benefits

in terms of selectivity, potentially minimizing interference from other electroactive species in complex samples. These findings underscore the versatility of metal nanocomplex-modified electrodes for arsenic detection. The high surface area and specific chemical interactions provided by these nanocomplexes contribute to their enhanced analytical performance, offering a promising platform for sensitive and selective arsenic quantification in environmental and analytical applications. The ability to tune the electrochemical properties through the choice of metal center provides additional flexibility in designing tailored sensing systems for specific analytical needs [44, 45].

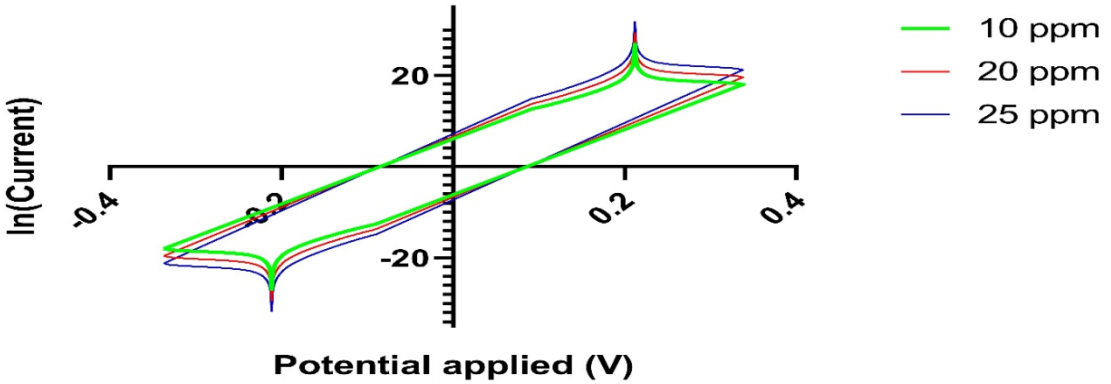

Fig. 7. Cyclic voltammograms of arsenic detection using Cu(II) and Fe(III) nanocomplex-modified electrodes at various concentrations (10, 20, and 25 ppm).

5.5. Efficient Removal of Carcinogenic Rose Bengal (RB) Dye Using Copper and Iron Nanocomplex

5.5.1. Adsorption Study of Rose Bengal (RB) Dye

5.5.1.1. Effect of Contact Time

The adsorption study of Rose Bengal (RB) dye using Cu(II) and Fe(III) nanocomplexes reveals interesting insights into their respective capabilities for dye removal from aqueous solutions [46-48]. Figure 8 illustrates the UV-visible absorption spectra of RB dye in the presence of Cu(II) and Fe(III) nanocomplexes over a contact time ranging from 5 to 50 minutes. For the Cu(II) nanocomplex (Figure 1), the initial spectrum of the RB dye shows a prominent absorption peak at approximately 550 nm. As the contact time increases, there is a significant decrease in the intensity of this peak, indicating the progressive removal of the dye from the solution. The adsorption process appears rapid, with a substantial reduction in peak intensity observed within the first 5 minutes. The adsorption progresses, albeit slower, up to 50 minutes, suggesting a gradual approach to equilibrium. The Fe(III) nanocomplex (Figure 2) demonstrates a similar trend but with some notable differences. The initial absorption peak of RB dye is also observed at around 550 nm, but the overall absorption intensity is lower than the Cu(II) system. This could indicate a lower initial concentration of RB dye or a difference in the spectrophotometric setup. The Fe(III) nanocomplex shows a rapid initial adsorption within the first 5 minutes, followed by a more gradual decrease in absorption intensity over the remaining period. Both Nano complexes exhibit a biphasic adsorption pattern, characterized by an initial rapid phase followed by a slower, more gradual phase. This behavior can be attributed to the abundance of readily available active sites on the nanocomplex surfaces at the onset of the process, followed by a gradual saturation of these sites as adsorption progresses. The Cu(II) nanocomplex demonstrates a higher overall adsorption capacity, as evidenced by the more significant reduction in peak intensity over time. This could be due to differences in surface area, pore structure, or specific interactions between the RB dye and the metal centres of the Nano complexes. For both Nano complexes, the adsorption process seems to approach equilibrium within 20-30 minutes, as indicated by the minimal changes in absorption spectra beyond this time point. This suggests that Cu(II) and Fe(III) Nano-complexes offer rapid adsorption kinetics, which is advantageous for practical applications in wastewater treatment. As suggested by their BET surface area analysis, the mesoporous nature of these Nano complexes likely contributes to their efficient adsorption properties. The presence of mesopores provides an optimal balance between surface area and accessibility, allowing for efficient diffusion and adsorption of dye molecules. In conclusion, both Cu(II) and Fe(III) Nano-complexes demonstrate promising capabilities for removing Rose Bengal dye from aqueous solutions. The Cu(II) nanocomplex has a slightly higher

adsorption capacity, while both complexes exhibit rapid adsorption kinetics. These characteristics make them potential candidates for environmental remediation applications, particularly in treating dye-contaminated wastewater streams. Further studies on the specific surface characteristics and adsorption mechanisms of these nanocomplexes could provide additional insights into optimizing their performance for dye removal applications.

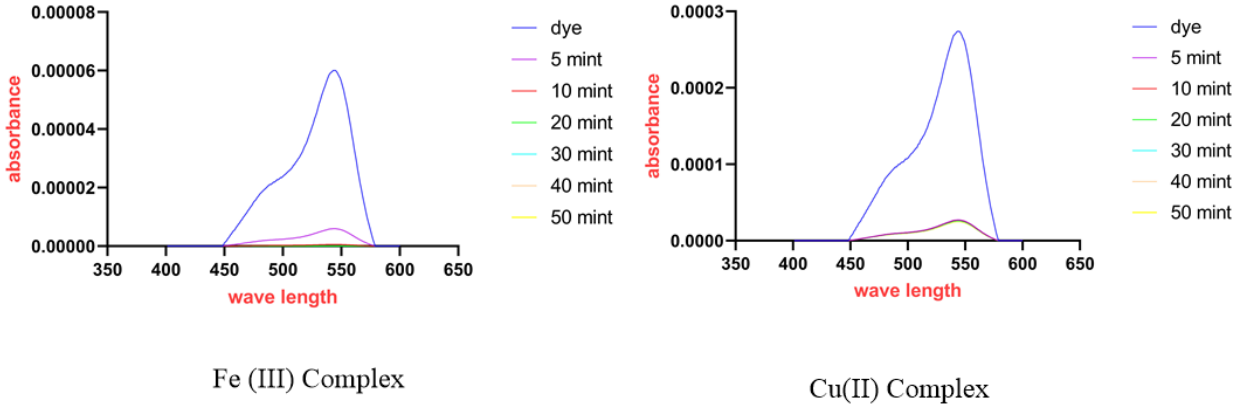

Fig. 8. Effect of time on removing Rose Bengal dye using Fe(III) and Cu(II) nanocomplex.

5.5.1.2. Effect of pH on the Adsorption of Rose Bengal Dye Using Copper Nanocomplex

The effect of pH on the adsorption of Rose Bengal dye using the Cu(II) nanocomplex reveals crucial insights into optimising the dye removal process [49]. Figure 9 illustrates the UV-visible absorption spectra of Rose Bengal dye in the Cu(II) nanocomplex presence at three different pH values: 4, 7, and 12. The spectra show a prominent absorption peak for Rose Bengal dye centred around 550 nm, characteristic of this dye. The intensity of this peak varies significantly with pH, indicating a strong dependence of the adsorption process on the solution's acidity or alkalinity. At pH 7 (neutral conditions), represented by the blue line, the absorption peak shows the highest intensity. This suggests that under neutral conditions, a significant amount of dye remains in the solution, indicating less effective Cu(II) nanocomplex adsorption. As the solution becomes acidic (pH 4, red line), there is a marked decrease in the absorption peak intensity. This reduction implies enhanced dye adsorption onto the Cu(II) nanocomplex surface. The improved adsorption efficiency in acidic conditions can be attributed to two main factors: protonation of the Cu(II) nano complex surface, creating more positively charged binding sites that attract the negatively charged dye molecules, and reduced competition from hydroxyl ions for adsorption sites on the nano complex surface. Conversely, at pH 12 (alkaline conditions), represented by the black line, the absorption peak shows the lowest intensity among the three pH values. This observation is somewhat unexpected and differs from the typical behavior of many adsorbents. It suggests that for this particular Cu(II) nanocomplex, strongly alkaline conditions also favor dye adsorption, albeit through a different mechanism than in acidic conditions. The enhanced adsorption in alkaline media could be due to the possible formation of Cu(II) hydroxide species on the nano complex surface, which might have a high affinity for the dye molecules or changes in the dye molecule's structure or charge state at high pH, potentially increasing its interaction with the nano complex. These results indicate that the Cu(II) nanocomplex exhibits a unique adsorption behavior, with increased efficiency at both low and high pH values and reduced effectiveness at neutral pH. This pH-dependent behavior provides valuable insights for applying the Cu(II) nanocomplex in dye removal processes. The ability of the Cu(II) nanocomplex to effectively adsorb Rose Bengal dye in both acidic and alkaline conditions offers flexibility in its application for wastewater treatment. It suggests that this adsorbent could be effective across various pH values, making it versatile for various industrial effluent conditions. However, it's important to note that while acidic and alkaline conditions enhance adsorption, extremely low or high pH values may not always be desirable from practical or environmental standpoints. Optimal pH conditions should balance maximum adsorption efficiency with considerations such as the stability of the adsorbent material, the potential for secondary pollution, and the ease of post-treatment processes. In conclusion, these findings provide valuable guidance for developing more effective and tailored wastewater treatment protocols using the Cu(II) nanocomplex. The unique pH-dependent behavior of this adsorbent opens up possibilities for its application in diverse environmental remediation strategies for dye-contaminated effluents.

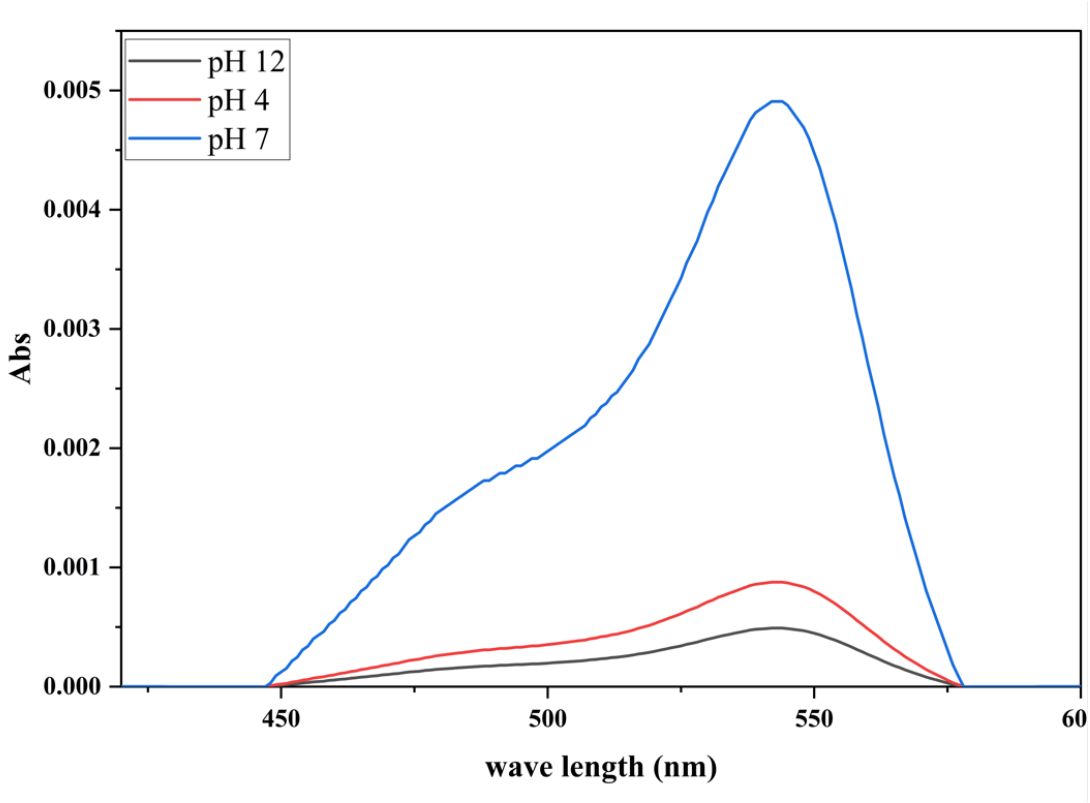

Fig. 9. UV-Visible absorption spectra of Rose Bengal Dye with Cu(II) nanocomplex at pH 4, 7, and 12.

5.5.1.3. Reusability Study of Hydrophobic Nanocomplex Adsorbent for Rose Bengal Dye Removal

The Cu(II) nanocomplex reusability for Rose Bengal dye removal was investigated to assess its practical applicability and economic viability in water treatment processes [50]. Figure 10 illustrates the results of multiple adsorption-desorption cycles, providing valuable insights into the regeneration capacity and long-term efficiency of the Cu(II) nanocomplex. The bar graph demonstrates the percentage of dye absorption over five consecutive recycle uses. Initially, the Cu(II) nanocomplex exhibited an impressive 90% absorption efficiency in its first use, highlighting its strong affinity for Rose Bengal dye. This high initial performance underscores the nanocomplex's potential as an effective adsorbent for dye removal in aqueous solutions. However, a gradual decrease in adsorption efficiency is observed over subsequent recycle uses. The second use shows a reduction to 60% absorption, followed by further declines to 45%, 35%, and 26% for the third, fourth, and fifth uses, respectively. This declining trend indicates that while the Cu(II) nanocomplex can be regenerated and reused, its performance diminishes with each cycle. The observed decrease in adsorption efficiency over multiple cycles can be attributed to several factors. These may include partially irreversible adsorption of dye molecules, gradual degradation of the nanocomplex structure, or accumulation of impurities on the adsorbent surface. Despite this decline, the Cu(II) nano complex maintains a removal efficiency of 26% even after five cycles, demonstrating its resilience and potential for repeated use in practical applications. The reusability study reveals the strengths and limitations of the Cu(II) nanocomplex as an adsorbent for Rose Bengal dye. Its high initial adsorption capacity and regenerative ability for multiple uses are significant advantages. These properties can reduce operational costs and minimise waste generation in large-scale water treatment operations. However, the substantial decrease in efficiency over successive cycles suggests that further optimization of the regeneration process may be necessary for long-term applications. Future research could focus on improving the regeneration method to maintain higher adsorption efficiencies over multiple cycles. This might involve exploring different desorption conditions, such as varying pH and temperature, or using mild regenerating agents that do not compromise the nanocomplex's structure. In conclusion, the Cu(II) nanocomplex demonstrates promising reusability characteristics for Rose Bengal dye removal, with a high initial adsorption capacity and the ability to maintain effectiveness over multiple cycles. While the decrease in efficiency with each reuse presents a challenge, the overall performance suggests that this material could be valuable in practical water treatment applications, especially in scenarios where periodic replacement or regeneration of the adsorbent is feasible. Further studies to enhance the regeneration process and extend the effective lifespan of the Cu(II) nanocomplex would be beneficial for optimizing its use in large-scale dye removal operations.

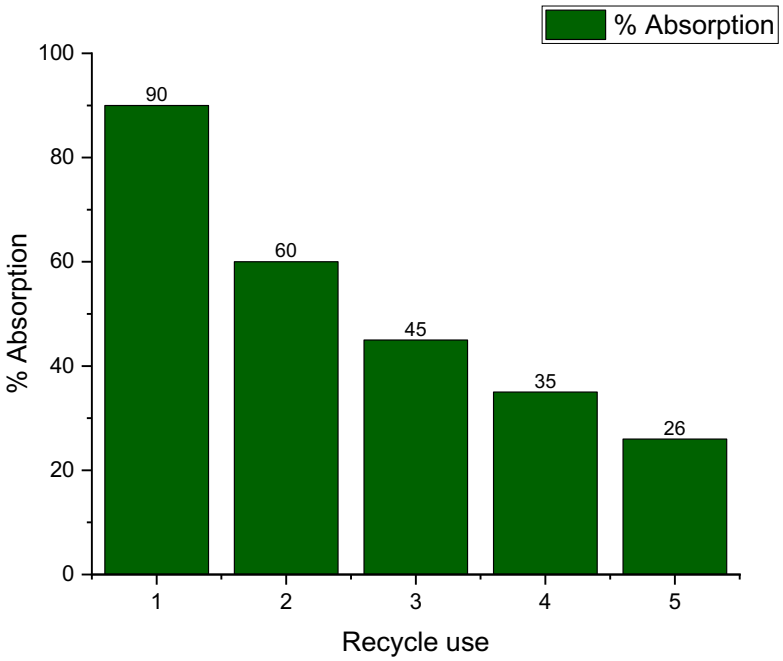

Fig. 10. Reusability study of Cu (II) nanocomplex for removal RB dye.

6. Conclusion

The synthesis and comprehensive characterization of novel Schiff base metal complexes have provided valuable insights into their structural, electronic, and functional properties. In particular, the Cu(II) and Fe(III) complexes demonstrated remarkable application versatility. Their nanostructured morphology and high surface areas contribute significantly to their efficacy in environmental remediation processes. The electrochemical detection of arsenic using these nanocomplexes offers a sensitive and selective method for monitoring this toxic element in water samples. Furthermore, the efficient removal of Rose Bengal dye by the Cu(II) complex and its unique pH-dependent adsorption behavior and reusability presents a promising solution for industrial wastewater treatment. The antimicrobial properties of these complexes also suggest potential applications in medicinal chemistry. While challenges such as decreased efficiency over multiple adsorption-desorption cycles were identified, the overall performance of these nano complexes underscores their potential for practical applications in environmental and analytical fields. Future research should focus on optimizing the regeneration processes and exploring additional applications of these versatile materials. This study contributes significantly to the growing knowledge of multifunctional metal complexes and their applications in addressing pressing environmental and analytical challenges.

Conflicts of interest

There are no conflicts to declare.

References

[1] Mansour, M. S. A., Abdelkarim, A. T., El-Sherif, A. A., & Mahmoud, W. H. (2024). Metal complexes featuring a quinazoline schiff base ligand and glycine: synthesis, characterization, DFT and molecular docking analyses revealing their potent antibacterial, anti-helicobacter pylori, and Anti-COVID-19 activities. BMC chemistry, 18(1), 150.

[2] Gaber, M., El-Ghamry, H. A., & Fathalla, S. K. (2015). Ni (II), Pd (II), and Pt (II) complexes of (1H-1, 2, 4-triazole-3-ylimino) methyl] naphthalene-2-ol. Structural, spectroscopic, biological, cytotoxicity, antioxidant, and DNA binding. *Spectrochimica Acta Part A: Molecular and Biomolecular Spectroscopy*, *139*, 396-404.

[3] Alaghaz, A. N. M., Zayed, M. E., Alharbi, S. A., Ammar, R. A., & Chinnathambi, A. (2015). Synthesis, spectroscopic identification, thermal, potentiometric and antibacterial activity studies of 4-amino-5-mercapto-S-triazole Schiff's base complexes. *Journal of Molecular Structure*, *1087*, 60-67.

[4] Saranya, J., Jone Kirubavathy, S., Chitra, S., Zarrouk, A., Kalpana, K., Lavanya, K., & Ravikiran, B. (2020). Tetradentate Schiff Base complexes of transition metals for antimicrobial activity. *Arabian journal for science and engineering*, *45*(6), 4683-4695.
[5] Dalia, S. A., Afsan, F., Hossain, M. S., Khan, M. N., Zakaria, C., Zahan, M. E., & Ali, M. (2018). A short review on chemistry of schiff base metal complexes and their catalytic application. *Int. J. Chem. Stud*, *6*(3), 2859-2867.
[6] El-Sonbati, A. Z., Mahmoud, W. H., Mohamed, G. G., Diab, M. A., Morgan, S. M., & Abbas, S. Y. (2019). Synthesis, characterization of Schiff base metal complexes and their biological investigation. *Applied Organometallic Chemistry*, *33*(9), e5048.
[7] Catalano, A., Sinicropi, M. S., Iacopetta, D., Ceramella, J., Mariconda, A., Rosano, C., ... & Longo, P. (2021). A review on the advancements in the field of metal complexes with Schiff bases as antiproliferative agents. *Applied Sciences*, *11*(13), 6027.
[8] Ejidike, I. P. (2018). Cu (II) Complexes of 4-[(1 E)-N-{2-[(Z)-Benzylidene-amino] ethyl} ethanimidoyl] benzene-1, 3-diol Schiff base: synthesis, spectroscopic, in-vitro antioxidant, antifungal and antibacterial studies. *Molecules*, *23*(7), 1581.
[9] Shah, S. S., Shah, D., Khan, I., Ahmad, S., Ali, U., & Rahman, A. (2020). Synthesis and antioxidant activities of Schiff bases and their complexes: An updated review. *Biointerface Res. Appl. Chem*, *10*(6), 6936-6963.
[10] Ibrahim, M. M., Fathy, A. M., Al-Harbi, S. A., Sallam, S. A., Al-Juaid, S. S., & Ramadan, A. E. M. M. (2021). Palladium (II) based imines; synthesis, characterization, X-ray structural analysis; DFT and catalytic hydrogenation study. Journal of Organometallic Chemistry, 939, 121764.
[11] Sumrra, S. H., Mushtaq, F., Khalid, M., Raza, M. A., Nazar, M. F., Ali, B., & Braga, A. A. (2018). Synthesis, spectral characterization and computed optical analysis of potent triazole based compounds. *Spectrochimica Acta Part A: Molecular and Biomolecular Spectroscopy*, *190*, 197-207.
[12] Adiguzel, R., Türkan, F., Yildiko, Ü., Aras, A., Evren, E., & Onkol, T. (2021). Synthesis and in silico studies of Novel Ru (II) complexes of Schiff base derivatives of 3-[(4-amino-5-thioxo-1, 2, 4-triazole-3-yl) methyl]-2 (3H)-benzoxazolone compounds as potent Glutathione S-transferase and Cholinesterases Inhibitor. *Journal of Molecular Structure*, *1231*, 129943.
[13] Abdel-Kader, N. S., Moustafa, H., El-Ansary, A. L., Sherif, O. E., & Farghaly, A. M. (2021). A coumarin Schiff base and its Ag (i) and Cu (ii) complexes: synthesis, characterization, DFT calculations and biological applications. *New Journal of Chemistry*, *45*(17), 7714-7730.
[14] Sangeetha, T. V., & Mohanapriya, S. (2021). Synthesis, characterization and biological evaluation of heterocyclic triazole derived Schiff base ligands comprising Mn (II) complexes: Implications of their DNA/protein binding docking and anticancer activity studies. *Indian Journal of Chemistry-Section A (IJCA)*, *60*(6), 797-805.
[15] Tyagi, P., Tyagi, M., Agrawal, S., Chandra, S., Ojha, H., & Pathak, M. (2017). Synthesis, characterization of 1, 2, 4-triazole Schiff base derived 3d-metal complexes: Induces cytotoxicity in HepG2, MCF-7 cell line, BSA binding fluorescence and DFT study. *Spectrochimica Acta Part A: Molecular and Biomolecular Spectroscopy*, *171*, 246-257.
[16] Benabid, W., Ouari, K., Bendia, S., Bourzami, R., & Ali, M. A. (2020). Crystal structure, spectroscopic studies, DFT calculations, cyclic voltammetry and biological activity of a copper (II) Schiff base complex. *Journal of Molecular Structure*, *1203*, 127313.
[17] Nimal, R. (2020). Electrochemical and spectroscopic characterization of biologically important Schiff bases. *SN Applied Sciences*, *2*, 1-12.
[18] Mansour, M. S. A., Abd-Elkarim, A. T., El-Sherif, A. A., & Mahmoud, W. H. (2024). Manganese, cobalt, and cadmium complexes of quinazoline schiff base ligand and methionine: synthesis, characterization, DFT, docking studies and biomedical application. *Egyptian Journal of Chemistry*, *67*(9), 479-506.
[19] Guideline, A. (2006). Clinical and Laboratory Standards Institute. *Wayne, PA*, *19*.
[20] Mansour, M. S., Ibrahium, A. T., El-Sherif, A. A., & Mahmoud, W. H. Organotin (IV) complexes: Synthesis, characterization, DFT, and molecular docking studies unveiling their potential biomedical uses. *Applied Organometallic Chemistry*, e7656.
[21] Mansour, M. S. A., Abd-Elkarim, A. T., El-Sherif, A. A., & Mahmoud, W. H. (2024). Manganese, cobalt, and cadmium complexes of quinazoline schiff base ligand and methionine: synthesis, characterization, DFT, docking studies and biomedical application. Egyptian Journal of Chemistry, 67(9), 479-506.
[22] Abo-Rehab, R.S., Kasim, E.A., Farhan, N., Tolba, M.S., Shehata, M.R. and Abdalla, E.M., (2024). Synthesis, characterization, anticancer, antibacterial, antioxidant, DFT, and molecular docking of novel La (III), Ce (III), Nd (III), and Dy (III) lanthanide complexes with Schiff base derived from 2-aminobenzothiazole and coumarin. Applied Organometallic Chemistry, 38(9), p.e7622.
[23] Abdel-Rahman, L.H., Alzarzah, S.F., Abdel-Hameed, M., Shehata, M.R. and El-Saghier, A., (2024). A new bio-active Schiff base ligand and its Ni (II), Cu (II), Ag (I), Zn (II), Cd (II), and La (III) binuclear complexes: synthesis, DFT analysis, antimicrobial, DNA interaction, COXII inhibition, and molecular docking studies. Applied Organometallic Chemistry, 38(9), p.e7631.
[24] Asran, A. M., Aldhalmi, A. K., Musa, E. N. A., Fayek, A. A., Mansour, M. S. A., & El-Sherif, A. A. (2024). Tridentate N-donor Schiff base metal Complexes: Synthesis, Characterization, computational Studies, and assessment of biomedical

applications in cancer Therapy, Helicobacter pylori Eradication, and COVID-19 treatment. Inorganic Chemistry Communications, 113371.
[25] Abd El-Halim, H. F., Mohamed, G. G., & Anwar, M. N. (2018). Antimicrobial and anticancer activities of Schiff base ligand and its transition metal mixed ligand complexes with heterocyclic base. Applied Organometallic Chemistry, 32(1), e3899.
[26] Abd El-Halim, H. F., & Mohamed, G. G. (2016). Synthesis, spectroscopic studies, thermal analyses, biological activity of tridentate coordinated transition metal complexes of bi (pyridyl-2-ylmethyl) amine] ligand. *Journal of Molecular Structure*, *1104*, 91-95.
[27] Abd El-Halim, H. F., Omar, M. M., & Anwar, M. N. (2017). Preparation, characterization, antimicrobial and anticancer activities of Schiff base mixed ligand complexes. *Journal of Thermal Analysis and Calorimetry*, *130*, 1069-1083.
[28] Creaven, B. S., Devereux, M., Foltyn, A., McClean, S., Rosair, G., Thangella, V. R., & Walsh, M. (2010). Quinolin-2 (1H)-one-triazole derived Schiff bases and their Cu (II) and Zn (II) complexes: Possible new therapeutic agents. Polyhedron, 29(2), 813-822.
[29] Aly, H. M., Moustafa, M. E., Nassar, M. Y., & Abdelrahman, E. A. (2015). Synthesis and characterization of novel Cu (II) complexes with 3-substituted-4-amino-5-mercapto-1, 2, 4-triazole Schiff bases: a new route to CuO nanoparticles. *Journal of Molecular Structure*, *1086*, 223-231.
[30] Abd El-Halim, H. F., & Mohamed, G. G. (2016). Synthesis, spectroscopic studies, thermal analyses, biological activity of tridentate coordinated transition metal complexes of bi (pyridyl-2-ylmethyl) amine] ligand. Journal of Molecular Structure, 1104, 91-95.
[31] El-Gammal, O. A., & Mostafa, M. M. (2014). Synthesis, characterization, molecular modeling and antioxidant activity of Girard′ s T thiosemicarbazide and its complexes with some transition metal ions. Spectrochimica Acta Part A: Molecular and Biomolecular Spectroscopy, 127, 530-542.
[32] Fahmy, O. M., Mahmoud, W. H., El Nashar, R. M., & El-Sherif, A. A. (2023). Nano Co (II) and Pd (II) Schiff base Complexes: Structural Characterization, Molecular docking, Antitumor proficiency and Biological evaluation. *Egyptian Journal of Chemistry*, *66*(13), 1373-1382.
[33] Mahmoud, W. H., Deghadi, R. G., El Desssouky, M. M., & Mohamed, G. G. (2019). Transition metal complexes of nano bidentate organometallic Schiff base: Preparation, structure characterization, biological activity, DFT and molecular docking studies. Applied Organometallic Chemistry, 33(1), e4556.
[34] Althagafi, I., El-Metwaly, N., & Farghaly, T. A. (2019). New series of thiazole derivatives: synthesis, structural elucidation, antimicrobial activity, molecular modeling and MOE docking. Molecules, 24(9), 1741.
[35] Fatma N. S., Walaa H. M., Omar M.M., Mohamed G.G. Theoretical studies of new Schiff base ligand derived from 1,3-diaminopropane and 2-acetyl ferrocene and studying some applications of its metal complexes, *Appl. Organometal. Chem*. 5143 (2019).
[36] Althagafi, I., El-Metwaly, N., & Farghaly, T. A. (2019). New series of thiazole derivatives: synthesis, structural elucidation, antimicrobial activity, molecular modeling and MOE docking. Molecules, 24(9), 1741.
[37] Iftikhar, B., Javed, K., Khan, M. S. U., Akhter, Z., Mirza, B., & Mckee, V. (2018). Synthesis, characterization and biological assay of Salicylaldehyde Schiff base Cu (II) complexes and their precursors. Journal of Molecular Structure, 1155, 337-348.
[38] Mansour, M. S. A., Abd-Elkarim, A. T., Mahmoud, W. H., & El-Sherif, A. A. (2024). QCM-Based Nano Schiff base Quinazoline-methionine hybrid ligand complex with Cobalt (II) as a Fast Response Nanosensor for instantaneous Monitoring water pollutant Pb (II) Ions. Egyptian Journal of Chemistry.
[39] Mansour, M. S. A., Abd-Elkarim, A. T., Mahmoud, W. H., & El-Sherif, A. A. (2024). Quinazoline-Glycine Manganese (II) Nano-Complex for Arsenic Sensing via QCM: Synthesis, Characterization, DFT Studies, Biological Evaluation and Environmental Application. *Egyptian Journal of Chemistry*.
[40] Mahmoud, W. H., Fayek, A. A., & El-Sherif, A. A. (2024). Chromium complex nanoparticles sensor for arsenic detection using QCM technique. Egyptian Journal of Chemistry, 67(5), 463-470.
[41] Mahmoud, W. H., Fayek, A. A., Taha, A., & El-Sherif, A. A. (2024). Synthesis, Textural and Thermal Properties of Nano Super Hydrophobic Cupper Complex as QCM Based Dye Sensor. Egyptian Journal of Chemistry, 67(4), 485-494.
[42] Zhou, M., Wei, Z., Qiao, H., Zhu, L., Yang, H., & Xia, T. (2009). Particle size and pore structure characterization of silver nanoparticles prepared by confined arc plasma. *Journal of Nanomaterials*, *2009*(1), 968058.
[43] Hwang, N., & Barron, A. R. (2011). BET surface area analysis of nanoparticles. *The connexions project*, 1-11.
[44] Alnuwaiser, M. A., & Rabia, M. (2024). Simple potentiometry and cyclic voltammetry techniques for sensing Hg 2+ ions in water using a promising flower-shaped WS 2-WO 3/poly-2-aminobenzene-1-thiol nanocomposite thin film electrode. RSC advances, 14(6), 3878-3887.
[45] Hamid Kargari, S., Ahour, F., & Mahmoudian, M. (2023). An electrochemical sensor for the detection of arsenic using nanocomposite-modified electrode. *Scientific Reports*, *13*(1), 8816.
[46] Gong, J. L., Wang, B., Zeng, G. M., Yang, C. P., Niu, C. G., Niu, Q. Y., ... & Liang, Y. (2009). Removal of cationic dyes from aqueous solution using magnetic multi-wall carbon nanotube nanocomposite as adsorbent. Journal of hazardous materials, 164(2-3), 1517-1522.

[47] Bhanvase, B. A., Sonawane, S., Pawade, V. B., & Pandit, A. B. (Eds.). (2021). *Handbook of nanomaterials for wastewater treatment: fundamentals and scale up issues*. Elsevier.
[48] Fadlalla, M. I., Senthil Kumar, P., Selvam, V., & Ganesh Babu, S. (2019). Recent advances in nanomaterials for wastewater treatment. *Advanced nanostructured materials for environmental remediation*, 21-58.
[49] Saad, R., Belkacemi, K., & Hamoudi, S. (2007). Adsorption of phosphate and nitrate anions on ammonium-functionalized MCM-48: effects of experimental conditions. Journal of colloid and interface science, 311(2), 375-381.
[50] Li, Z. Z., Liou, T. H., Liu, W. Y., Hsu, C. C., & Chiu, S. E. (2023). Characterization of new modified mesostructured silica nanocomposites fabricated for effective removal of aromatic acids. Arabian Journal of Chemistry, 16(10), 105145.